COMPUTATION OF MULTIPHASE FLOW BY VOLUME OF FLUID AND HIGH-ORDER FRONT TRACKING METHODS

Stéphane Zaleski

Modélisation en Mécanique, UMR CNRS 7607,
Université Pierre et Marie Curie – Paris 6,
Paris, France. *zaleski@lmm.jussieu.fr*

Contents

1 Introduction

The numerical simulation of flows with interfaces and free-surface flows is an extremely vast topic, with applications to domains as varied as fluid mechanics applied to the environment, geophysics, engineering or fundamental physics.

To select a particular topic in engineering, among many others, the study of liquid-gas interfaces is quite important in combustion problems with liquid and gas reagents. The formation of droplet clouds or sprays that subsequently burn in combustion chambers originates in interfacial instabilities, such as the Kelvin-Helmholtz instability. What can numerical simulation do to improve our understanding of these phenomena? At first look it is of little help. The limitations of numerical techniques make it impossible to consider more than a few droplets or bubbles. They also force us to stay at rather low Reynolds or Weber numbers. These limitations prevent us from finding a direct solution to the breakup problem. However, these methods are potentially very important. For one, the continuous improvement of computational power (or, what amounts to the same, the drop in megaflop price) continuously extends the range of affordable problems. Second, and more deeply, the phenomena we consider often happen on space and time scales where experimental visualization is difficult or impossible in practice. Numerical simulation may here be a useful prod to the intuition of the physicist, the engineer or the mathematician.

A typical example of interfacial flow is the collision between two liquid droplets. Finding the flow not only involves the study of hydrodynamic fields in the air and water phases, but also of the air-water *interface*. This latter part is much more difficult than the former because the interface is subject to a number of relevant physical phenomena, at scales much smaller than the typical sizes of the droplets. For instance, a severe difficulty is the change in interface topology that occurs when the colliding droplets coalesce. This considerably complicates the physics and sharpens the requirements that a numerical method must satisfy in order to resolve the motion in a satisfactory way.

These difficulties are dealt with in a variety of manners depending on the physical modeling and the numerical methods. First comes a choice of modeling the interface as a sharp or thick region of space. In engineering problems, such as combustion studies, the interface may be considered a discontinuity of density and pressure as well as some other physical variables. The location of this discontinuity in three-dimensional space will be assumed to be a two-dimensional, twice-differentiable manifold (to simplify, a smooth surface S) which evolves according to pre-determined rules.

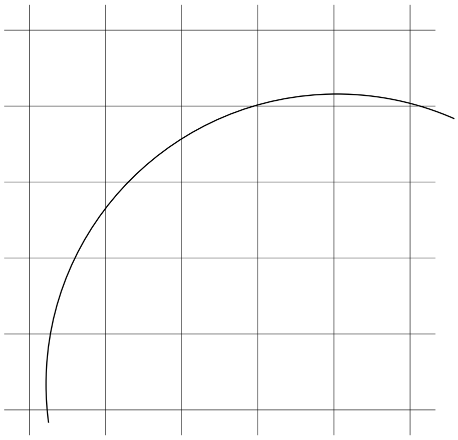

Figure 1: An interface cutting across a fixed, structured grid.

Our second choice is to decide which forces and thermal effects we want to model. The main thrust of this lecture is as follows. In the bulk of the fluids, we shall restrict ourselves to viscosity, constant in each phase, and perhaps gravity. On interfaces, we shall assume a constant surface tension. Our physical assumptions thus lead us to a version of the Navier-Stokes equation, with variable density and viscosity and capillary tension on S. This should be contrasted with both a more elementary approach, in which only perfect fluids are considered, and many more complex approaches where more realistic theories of interfaces or other transport effects (involving temperature, passive scalars or surface-active substances) are considered.

Once this framework is set, we have to attack the subject matter of this lecture: simulation methods for the Navier-Stokes equation with interfaces. On one hand the numerical methods are analogous to otherwise well-known methods in the bulk of the phases such as finite elements, finite volumes, finite differences. On the other hand, there are specific problems due to the presence of the interface: location of the discontinuity, computation of surface stresses.

From this point of view the various methods for interface simulation divide in two great classes, depending on the nature, fixed or moving, of the grid used in the bulk of the phases. In *fixed-grid methods*, there is a predefined grid that does not move with the interface. The interface has to somehow cut across this fixed grid. As shown on figures 1 and 2 this fixed grid may be either structured on unstructured. In *moving-grid methods*, the interface is a boundary between two sub-domains of the grid. The interface then identifies, at some order of approximation, with element boundaries. Again, the grid may be structured and even near-orthogonal, or more general. This simplifies

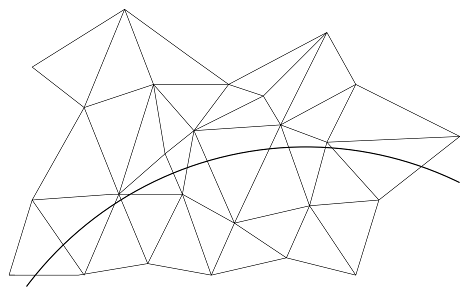

Figure 2: An interface cutting across a fixed, unstructured grid.

the analysis near the interface. However when the interface undergoes large deformations the grid has to be remeshed. Other complications, especially when the topology changes, may occur. In addition to the moving-grid and fixed-grid methods, there are special cases in which grids are not needed, such as particle methods.

In this article we put emphasis on fixed-grid methods. These are more interesting for us because of their relatively simple description and greater ease of programming. Easier extension to three dimensions of space is one of the principal advantages expected from this simplified formulation. Moreover, most of the lecture is concerned with so-called Volume-of-Fluid (VOF) methods. Many commercially available codes use this method to represent interfaces: SOLA-VOF(Nichols et al., 1980), NASA-VOF2D(Torrey et al., 1985), NASA-VOF3D(Torrey et al., 1987), RIPPLE(Kothe and Mjolsness, 1992) and FLOW3D.

This lecture remains at a rather introductory level. The reader may read with profit some other reviews and books (Floryan and Rasmussen, 1989; Shyy et al., 1996; Sethian, 1996; Rothman and Zaleski, 1997). The review of Mc Hyman (1984) is particularly clear, pleasant to read and still refreshing, as well as informative to the novice practitioner.

The present lecture reflects my personal point of view: some aspects of the subject have been emphasized, others have been omitted. For instance, interface simulation using boundary integral methods is not described in detail, only relevant references are given below. Similarly, lattice-gas and Boltzmann-lattice-gas methods are described in other reviews and books. (Rothman and Zaleski, 1994; Rothman and Zaleski, 1997; Benzi et al., 1992) The same holds for level-set methods (Sussman et al., 1994; Sethian, 1996; Sussman and Smereka, 1997).

2 Physical and mathematical modeling of interfaces

Fluid mechanics with sharp interfaces between phases are introduced in this Chapter. The various formulations of the basic equations are derived from first principles, in order to point out clearly all the underlying assumptions. The equations can take various forms and in numerical work we will find that it often makes a difference what form we use for a particular problem.

We will work solely with the continuum theory of fluids, and thus use *conservation* principles, supplemented by *constitutive* assumptions about the nature of the fluids and the interfaces between them. The approximation of vanishingly thin, sharp interfaces plays an important rôle. The conservation principles are common to any material but different constitutive hypothesizes apply to different materials. Expressing the basic principles of conservation of mass, momentum, and energy in mathematical form leads to the governing equations for fluid flow.

We place particular emphasis on incompressible flows. However a wider discussion of compressible flow equations can be found in Appendix ...

2.1 General principles

We base our derivation on three general principles: the continuum hypothesis, the hypothesis of sharp interfaces, and the neglect of intermolecular forces.

The approximation of a fluid as a continuum is a fundamental principle of fluid mechanics. This assumption will be valid in most practical cases. Indeed, real fluids are made of atoms or molecules, and are discontinuous. Consider for instance the amount of mass per unit volume, or density ρ. If this amount was measured in a box of small dimensions ℓ, it would be a wildly fluctuating quantity (see (Batchelor, 1970) for a detailed discussion). However as the box size ℓ increases the density appears ever smoother, until it is well approximated by a smooth function ρ. For liquids in ambient conditions this happens above a few tens of nanometers (1 nm $= 10^{-9}$ m). In some cases such as dilute gases the discrete nature of matter may be felt over much longer lengths. For dilute gases the average distance between molecular collisions or *mean free path* of the gas $\ell_{\rm mfp}$ is what counts. The gas then obeys the Navier-Stokes equations on scales $\ell \gg \ell_{\rm mfp}$.

Beyond the continuum hypothesis, we shall make the *assumption of sharp interfaces*. Interfaces separate different thermodynamic phases, such as air and water, oil and vinegar, or any two *immiscible* fluids. The properties of fluids such as equation of state, density, viscosity, heat conductivity vary from phase to phase. The transition from one phase to another occurs on very small scales, comparable to the scales of a few tenth of nanometers described above. Thus we may safely assume that the interfaces have vanishing thickness.

We also make some restrictions on the type of forces that may occur. Long range forces between fluid particles, such as electromagnetic forces in charged fluids shall not be considered. The intermolecular forces, such as Van der Waals forces (for further references see) that play an important role in interface physics, are modelled by retaining their most important effect, capillarity. This effect, also called surface tension force, amount to a stress concentrated on the sharp interfaces.

The three assumptions above also reflect the fact that it would be near impossible, in the current state of the art, to describe complex droplet and bubble interactions while keeping the microscopic physics. For instance, simulating physical phenomena from the nanonmeter to the centimeter scale would require 10^7 grid points in every direction, a clearly impossible feat.

Beyond the three assumptions above, we mostly deal in this coursewith incompressible flow. This is because taking into account compressibility puts severe numerical constraints on the simulations.

2.2 Basic equations

One way to introduce the basic equations is to state them as conservation laws. The principle of conservation of mass states that mass can not be created nor destroyed. Therefore, if we consider a volume fixed in space V, then the change of mass inside this volume can only take place if mass flows in or out through the boundary of this volume, S. The flow out of the volume through a surface element ds is $\rho\ \mathbf{u}\cdot\mathbf{n}ds$ where $\mathbf{n}$ is the outward normal, ρ the density and $\mathbf{u}$ the velocity. Stated in integral form

$$\frac{d}{dt}\int_V \rho dv = -\oint_S \rho\mathbf{u}\cdot\mathbf{n}ds,$$

Here, the left hand side is the rate of change of mass in the volume V and the right hand side represents in and out flow through the boundaries of V. Since the volume is fixed in space we can take the derivative inside the integral, and by applying the divergence theorem to the boundary fluxes on the right hand side we have

$$\int_V \left[\frac{\partial\rho}{\partial t} + \nabla\cdot(\rho\mathbf{u})\right] dv = 0.$$

This must hold for any arbitrary volume, no matter how small, and thus must also hold at a point, if the flow field is smooth. The partial differential equation expressing conservation of mass is therefore:

$$\frac{\partial \rho}{\partial t} + \nabla \cdot (\rho \mathbf{u}) = 0$$

By using the definition of the substantial derivative

$$\frac{D()}{Dt} = \frac{\partial()}{\partial t} + \mathbf{u} \cdot \nabla(),$$

the continuity equation can be rewritten as

$$\frac{\partial \rho}{\partial t} + \mathbf{u} \cdot \nabla \rho + \rho \nabla \cdot \mathbf{u} = \frac{D\rho}{Dt} + \rho \nabla \cdot \mathbf{u} = 0.$$

The equation of motion is derived by assuming that the rate of change of momentum of a fixed volume is the difference in momentum flux across the boundaries of the volume plus the net forces acting on the volume. Therefore

$$\frac{d}{dt} \int_V \rho \mathbf{u} dv = -\oint_S \rho \mathbf{u}(\mathbf{u} \cdot \mathbf{n}) ds + \int_V \rho \mathbf{f} dv + \oint_S \mathbf{n} \cdot \mathbf{T} ds.$$

The first term on the right-hand side is the momentum flux through the boundary of V, and the next terms are the body forces $\mathbf{f}$, and surface forces, respectively. $\mathbf{T}$ is a symmetric stress tensor constructed in such a way that $\mathbf{n} \cdot \mathbf{T} ds$ are the forces on the element ds of normal $\mathbf{n}$ of the surface S bounding V.

By the same arguments as applied to the mass conservation equation this must be valid at every point in the fluid, so

$$\frac{\partial \rho \mathbf{u}}{\partial t} = -\nabla \cdot (\rho \mathbf{u} \otimes \mathbf{u}) + \rho \mathbf{f} + \nabla \cdot \mathbf{T}.$$

Here, $\mathbf{a} \otimes \mathbf{b}$ is the tensor product whose ij-th component is $a_i b_j$. Thus for instance $\mathbf{u} \otimes \mathbf{u}$ has ij-th component $u_i u_j$. The nonlinear term can be written as

$$\nabla \cdot (\rho \mathbf{u} \otimes \mathbf{u}) = \rho \mathbf{u} \cdot \nabla \mathbf{u} + \mathbf{u} \nabla \cdot (\rho \mathbf{u}).$$

Using the definition of the substantial derivative and the continuity equation we can rewrite the above equation as

$$\rho \frac{D\mathbf{u}}{Dt} = \rho \mathbf{f} + \nabla \cdot \mathbf{T}.$$

This is Cauchy's equation of motion and is valid for any continuous medium. For fluids like water, oil, and air (as well as many others that are generally

$$\frac{d}{dt}\int_V \rho dv + \oint_S \rho \mathbf{u}\cdot\mathbf{n}ds = 0$$

$$\frac{d}{dt}\int_V \rho\mathbf{u}dv = \int_V \rho\mathbf{f}dv + \oint_S \Big(\mathbf{nT} - \rho\mathbf{u}(\mathbf{u}\cdot\mathbf{n})\Big)ds$$

Figure 3: The equations of fluid motion in integral form. The flux terms have been moved under the same surface integral as the stress terms.

$$\frac{\partial\rho}{\partial t} + \nabla\cdot(\rho\mathbf{u}) = 0$$

$$\frac{\partial\rho\mathbf{u}}{\partial t} = \rho\mathbf{f} + \nabla\cdot(\mathbf{T} - \rho\mathbf{uu})$$

Figure 4: The equations of fluid motion in conservative form.

referred to as Newtonian fluids) the stress may be assumed to be a linear function of the rate of strain, or

$$\mathbf{T} = (-p + \lambda\nabla\cdot\mathbf{u})\mathbf{I} + 2\mu\mathbf{D}$$

where $\mathbf{I}$ is the unit tensor and $\mathbf{D} = \frac{1}{2}(\nabla\mathbf{u} + \nabla\mathbf{u}^T)$ is the deformation tensor whose components are

$$D_{ij} = \frac{1}{2}\Big(\frac{\partial u_i}{\partial x_j} + \frac{\partial u_j}{\partial x_i}\Big).$$

Here, λ is the second coefficient of viscosity, and if Stokes' hypothesis is assumed to hold then $\lambda = -(2/3)\mu$. [1] Substituting the expression for the stress tensor into Cauchy's equation of motion results in

$$\rho\frac{D\mathbf{u}}{Dt} = \rho\mathbf{f} - \nabla p + \nabla(\lambda\nabla\cdot\mathbf{u}) + \nabla\cdot(2\mu\mathbf{D}). \tag{1}$$

If the viscosity is a constant, the last term is simply $\mu\nabla^2\mathbf{u}$.

2.3 Incompressible Flows

For an important class of flows the density of a material particle does not change as it moves with the flow. This is gernerally the case when the flow

[1] In several texts the discussion is based on the bulk viscosity $\kappa = 2/3\mu + \lambda$. Stokes' hypothesis is that the bulk viscosity vanishes.

velocity U is smaller than sound velocity c_s, that is when the Mach number Ma $= U/c_s$ is much smaller than unity.

The equation of mass conservation is therefore

$$\frac{D\rho}{Dt} = \frac{\partial \rho}{\partial t} + \mathbf{u} \cdot \nabla \rho = 0$$

and the continuity equation reduces to

$$\nabla \cdot \mathbf{u} = 0.$$

This states that the volume of any fluid element can not be changed and these flows are therefore called incompressible flows. By expanding the divergence in (2) and using the equation of state we find that

$$\oint_S \mathbf{u} \cdot \mathbf{n} ds = 0$$

for incompressible flows. Notice that there is no restriction to constant density flows here, the density of a material particle can vary from one particle to the next one, but the density of each particle must stay constant. The density field is found by solving the equation of state, eq. (6), but if the density is constant everywhere that is not necessary.

The special case of incompressible fluids with constant density and viscosity is of considerable importance, and we will devote much space to that. The equations to be solved are then (2.3) and

$$\frac{\partial \mathbf{u}}{\partial t} + \mathbf{u} \cdot \nabla \mathbf{u} = -\frac{\nabla p}{\rho} + \mathbf{f} + \nu \nabla^2 \mathbf{u}$$

where $\nu = \mu/\rho$ is called the kinematic viscosity. This is the form usually seen in text books, but we note that the nonlinear term can be expressed in several forms:

$$\mathbf{u} \cdot \nabla \mathbf{u} = \nabla \cdot (\mathbf{u} \otimes \mathbf{u}) = \frac{1}{2} \nabla (\mathbf{u} \cdot \mathbf{u}) - \mathbf{u} \times (\nabla \times \mathbf{u}).$$

For numerical predictions equations (2.3) and (2.3) are actually somewhat awkward: We have evolution equations for each of the velocity component, and one expression for the relation between the velocities but really no separate equation for the pressure. This can be corrected by taking the divergence of the momentum equation and using the incompressibility conditions to eliminate the time derivative. This leads to

$$\nabla^2 p = -\rho \nabla \cdot (\mathbf{u} \cdot \nabla \mathbf{u}) + \nabla \cdot \mathbf{f}$$

Here goes a figure of the slip velocity

Figure 5: Slip velocity

which replaces the incompressibility equation. We note the special role played by the pressure for incompressible fluid. Instead of being a thermodynamic function of (say) density and temperature, it is determined solely by the velocity field. Indeed, it will take on whatever value is necessary to make the flow divergence free. It is sometimes convenient—and we will use this extensively—to think of the pressure as projecting the velocity field into the space of incompressible functions. That is, we imagine the velocity first being predicted by (2.3) without the pressure, then we adjust the pressure in such a way as to enforce incompressibility and correct the velocities.

The Navier-Stokes equations for variable density and viscosity, in conservative form, are:

$$\frac{\partial \rho \mathbf{u}}{\partial t} + \nabla \cdot \rho \mathbf{u}\mathbf{u} = -\nabla p - \rho g \hat{k} + \nabla \cdot (2\mu \mathbf{D}) + \mathbf{f}$$

where

$$\mathbf{D} = \frac{1}{2}(\nabla \mathbf{u} + \nabla \mathbf{u}^T).$$

2.3.1 Boundary conditions

One of the major difficulty with numerical simulations of fluid flow is the correct implementation of the boundary conditions. In principle the conditions at boundaries are well defined. For viscous, incompressible fluids we require that the fluid sticks to the wall so the fluid velocity there is equal to the wall velocity

$$\mathbf{u} = \mathbf{U}_{wall}$$

.

This does not cause special difficulties with the notable exception of moving contact lines. In that case, it has sometimes been suggested that the solid wall condition should be replaced by a condition allowing a degree of slip, such as

$$\mathbf{u} - \mathbf{U}_{wall} = k \frac{\partial \mathbf{u}}{\partial n}$$

where k is a slip coefficient, with the dimensions of a (small) length and $\frac{\partial ()}{\partial n}$ is the derivative in the direction normal to the wall. The slip length is the distance at which the velocity would vanish if extrapolated inside the wall (Fig. 5).

Here goes a figure of the height function.

Figure 6: Height function and the problem of overhangs

2.4 Interfaces: definitions and geometry

In three-dimensional space, the locus of the interface is a smooth surface S which separates the two fluid phases. In two dimensions, the interface is a line C. We start with lines and expose various ways of defining an interface. A more systematic description of interface geometry may be found in Aris (1962) (Aris, 1962). Numerical methods often derive from each specific way to define an interface.

2.4.1 Two-dimensional geometry

The simplest way to define a line is through an equation of the form

$$y = h(x, t). \tag{2}$$

For instance for an ellipse

$$y = \pm b(1 - x^2/a^2)^{1/2} \tag{3}$$

The normal vector is then

$$\mathbf{n} = \left[1 + \left(\frac{\partial h}{\partial x}\right)^2\right]^{-1/2} \left(-\frac{\partial h}{\partial x}, 1\right)$$

and curvature is

$$\kappa = \frac{\partial^2 h}{\partial^2 x}\left[1 + \left(\frac{\partial h}{\partial x}\right)^2\right]^{-3/2}$$

These definitions are convenient but may pose problems when the interface has overhangs (figure 6).

In a coordinate-independent way, a line may be described by a vector function $\mathbf{x}(u)$ of a real parameter u. The tangent vector is $d\mathbf{x}/du$. Again for the ellipse

$$\begin{aligned} x &= a\cos u \\ y &= b\sin u \end{aligned} \tag{4}$$

It is often useful to work with a curve parameterization that conserves length. Then the parameter is called the curvilinear abcissa s and is chosen such that $||d\mathbf{x}/ds|| = 1$, the tangent is the unit tangent, noted $\mathbf{t}$. The normal to the interface is defined as follows. Consider a drop of phase "1" surrounded by

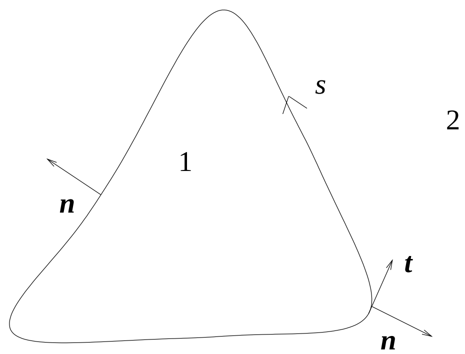

Figure 7: Some notations for a 2D interface are defined on this figure. The unit normal is always from phase 1 to phase 2.

phase “2” (Figure 7). We chose the curvilinear coordinate s so that one rotates counterclockwise around the drop. The normal is then defined as the unit vector perpendicular to $\mathbf{t}$ and is directed towards the outside of the drop. The unit normal and the unit tangent are related by

$$\mathrm{d}\mathbf{t}/\mathrm{d}s = -\kappa\mathbf{n} \tag{5}$$

where κ is the curvature. Its modulus is $|\kappa| = ||\mathrm{d}\mathbf{t}/\mathrm{d}s||$. In this case its sign is positive where the "inside" (phase 1) region is convex and negative where it is concave, but the sign of the curvature depends on the direction chosen for the normal. As another definition of curvature, we have $|\kappa| = 1/R$ where R, the radius of curvature, is the radius of the osculating circle to the curve, i.e. of the circle that most closely approximates the curve. For a circle, the curvature is positive and exactly $1/R$. Another way to define the interface is through a level-set function F. We chose for $F(x, y)$ any smooth function such that the interface is located on the level set

$$F(x, y) = 0. \tag{6}$$

The ellipse may be described by the level set function

$$F = \frac{x^2}{a^2} + \frac{y^2}{b^2} - 1. \tag{7}$$

Using the level set function provides a simple formula for the unit normal

$$\mathbf{n} = \nabla F/||\nabla F|| \tag{8}$$

and the curvature is

$$\kappa = \nabla \cdot \mathbf{n} \tag{9}$$

To prove the above relation, notice that the divergence of a vector $\mathbf{u}$ is

$$\nabla \cdot \mathbf{u} = \mathbf{t} \cdot \frac{\partial}{\partial s}\mathbf{u} + \mathbf{n} \cdot \frac{\partial}{\partial n}\mathbf{u}. \tag{10}$$

We also notice that since $\mathbf{n}$ is of constant length, it is perpendicular to its derivative and $\mathbf{n} \cdot \frac{\partial}{\partial n}\mathbf{n} = 0$. Applying (10) to $\mathbf{n}$ we get

$$\nabla \cdot \mathbf{n} = \mathbf{t} \cdot \frac{\partial}{\partial s}\mathbf{n} \tag{11}$$

then using (5) we recover (9). Yet another useful device is the characteristic function H such that $H = 1$ in phase 1 and $H = 0$ in phase 2. For instance for the ellipse we take

$$H = H_1\left(\frac{x^2}{a^2} + \frac{y^2}{b^2} - 1\right) \tag{12}$$

where H_1 is the one-dimensional Heaviside step function. It is convenient to express H in terms of an integral over the product of one-dimensional δ-functions:

$$H(x, y, t) = \int_{A(t)} \delta(x - x')\delta(y - y')da'. \tag{13}$$

.

2.4.2 Three-dimensional geometry

The previous methods all carry over to the three dimensional case. The height function defines the interface through the *Monge parameterization*

$$z = h(x, y, t). \tag{14}$$

Alternately the interface may be defined by an arbitrary parameterization

$$(\xi_1, \xi_2) \longrightarrow \mathbf{x}(\xi_1, \xi_2, t) = (x, y, z) \tag{15}$$

The coordinates ξ_1, ξ_2 form a set of intrinsic coordinates for the interface. For a small variation of the coordinates ξ_i we have a small variation $d\mathbf{x}$ of the position. The distance covered by $\mathbf{x}$ is $ds^2 = (d\mathbf{x})^2$. The metric tensor g_{ij} is defined by

$$\mathrm{d}s^2 = g_{ij}(\xi_1, \xi_2, t)\, \mathrm{d}\xi^i\, \mathrm{d}\xi^j \tag{16}$$

where $\mathrm{d}s^2$ is the length element corresponding to a variation $\mathrm{d}\xi^i$ of the coordinates. The *metric* is $g = g_{11}g_{22} - g_{12}^2$. When the metric tensor is unity the coordinate system is orthonormal. For surface in 3D space, it is customary to note u, v the parameters and E, F and G the components of the metric tensor:

$$\mathrm{d}s^2 = E\mathrm{d}u^2 + F\mathrm{d}u\mathrm{d}v + G\mathrm{d}v^2 \tag{17}$$

The system is orthogonal when $F = 0$ and orthormal when in addition $E = F = 1$. It is not possible in general to have an orthonormal coordinate system adapted to an arbitrary interface. However for some definitions we shall find useful to think in terms of a locally orthonormal system, that is a system for which $E = G = 1$, $F = 0$ for a given point of coordinates ξ^i. Other descriptions of the interface in 2D, such as the level set function are naturally extended to 3D and so is the characteristic function H, for which we have:

$$H(x, y, z, t) = \int_{V(t)} \delta(x - x')\delta(y - y')\delta(z - z')dv' \tag{18}$$

over the volume $V(t)$ of phase 1.

A surface in three-dimensional space has two principal curvatures

$$\kappa_1 = 1/R_1 \qquad \text{and} \qquad \kappa_2 = 1/R_2.$$

A simple definition of these curvatures is to consider a coordinate system such that, near the origin the surface is approximated by

$$z = \frac{1}{2}(\kappa_1 x^2 + \kappa_2 y^2) + \mathrm{O}\ \left((x^2 + y^2)^2\right) \tag{19}$$

The first curvature is then

$$\kappa = \kappa_1 + \kappa_2$$

(Some authors call κ the mean curvature and/or include a factor 1/2 in the definition, in this book we may use the term mean curvature but omit the 1/2 factor). The second (or total, or Gauss) curvature is the product of the principal curvatures

$$\kappa_{\mathrm{Gauss}} = \kappa_1\kappa_2. \tag{20}$$

Using a level-set formulation is just as in the 1D case

$$F(x, y, z, t) = 0 \tag{21}$$

defines the surface. An example using the Monge parameterisation is $F = z - h(x, y, t)$. The definition of the normal (8) is just as true in 3D, and (9) may be used to define the mean curvature. It is also useful to have a definition of the surface gradient $\nabla_S\phi$ of a scalar quantity ϕ defined on the surface, as well as the surface divergence $\nabla_S \cdot \mathbf{v}$ of a surface vector or a space vector $\mathbf{v}$. The general definition of the ∇ operator on a surface is somewhat complex (see notes) but for a locally orthonormal system ξ_1, ξ_2 it is simple. The operator is noted ∇_S to distinguish it from the 3D operator and

$$\nabla_S = \mathbf{t}_1 \frac{\partial}{\partial \xi_1} + \mathbf{t}_2 \frac{\partial}{\partial \xi_2}. \tag{22}$$

Then the mean curvature is also the surface divergence of $\mathbf{n}$

$$\kappa = \nabla_S \cdot \mathbf{n} \tag{23}$$

2.4.3 Distributions concentrated on the interface

It is useful to define a function δ_S that is concentrated the interface just as Dirac δ-function is concentratred on a point. The surface distribution δ_S is conveniently related to the gradient of H. We note first that since the gradient in Eq. (13) is with respect to the unprimed variables, the gradient operator can be put under the integral sign

$$\nabla H = \int_A \nabla \left[\delta(x - x')\delta(y - y')\right] da'. \tag{24}$$

Since the δ-functions are anti-symmetric with respect to the primed and unprimed variables, the gradient with respect to the unprimed variables can be replaced by the gradient with respect to the primed variables.

$$`\nabla H = -\int_A \nabla' \left[\delta(x - x')\delta(y - y')\right] da' \tag{25}$$

The resulting area (or volume in three-dimensions) integral can the be transformed into a line (surface) integral by a variation of the divergence theorem for gradients

$$\nabla H = -\oint_S \delta(x - x')\delta(y - y')\mathbf{n} ds'.$$

where the prime on the gradient symbol denotes the gradient with respect to the primed variables. Although we have assumed that the area occupied by the marked fluid is finite so that S is a closed contour, the contribution of most of the integral is zero so we can replace it by one over a part of the contour and drop the circle on the integral:

$$\nabla H = -\int_S \delta(x - x')\delta(y - y')\mathbf{n} ds' \tag{26}$$

This is readily generalized to three dimensions where we have

$$\nabla H = -\int_S \delta(x - x')\delta(y - y')\delta(z - z')\mathbf{n} ds' \tag{27}$$

This may yet be noted

$$\nabla H = -\delta_S \mathbf{n} \tag{28}$$

The function δ_S has the property of changing volume integrals into surface integrals. For any function f

$$\int_A \delta_S(\mathbf{x}) f(\mathbf{x}) da = \int_S f(\mathbf{x}) ds \tag{29}$$

Using a locally orthonormal coordinate system ξ_1, ξ_2, n where n is as usual the coordinate normal to the interface, we have

$$\delta_S(\mathbf{x}) = \delta(n) \tag{30}$$

where δ is the ordinary Dirac distrubution.

2.4.4 Interface motion

The evolution of the interface S is defined by a specified normal velocity $V(\xi_1, \xi_2, t)$, on each point of S. This may be the fluid velocity itself, or a result of other effects, such as evaporation or condensation. In parametric form

$$\mathbf{n} \cdot \partial_t \mathbf{x}(\xi_1, \xi_2, t) = V(\xi_1, \xi_2, t) \tag{31}$$

where $\mathbf{n}$ is the normal vector to the interface. The tangential velocity is left arbitrary. When the interface is described by marker particles this means that the tangential velocity of the markers is irrelevant.

Other descriptions of the motion are often more useful. For instance if the interface is described by a level set function F, a specific trick may be to extend the velocity field to the entire space in some smooth manner. Then the idea that a particle on the interface follows the velocity field may be expressed by

$$\frac{DF}{Dt} = 0. \tag{32}$$

This description may also hold for the characteristic function H although now the derivatives must be understood in a weak sense.

$$\frac{DH}{Dt} = 0. \tag{33}$$

The Monge parameterization 14 is related to the level set function by

$$F = h(x, y, t) - z. \tag{34}$$

Applying eq. (32) we get

$$\partial_t h + u \partial_x h + v \partial_y h - w = 0, \tag{35}$$

or yet

$$\frac{dh}{dt} = w \tag{36}$$

where $d/dt = \partial_t + u\partial_x + v\partial_y$ is the 2D total derivative.

2.5 Fluid mechanics with interfaces

We consider the incompressible flow of two immiscible liquids. The whole flow fills a domain Ω. This domain may be decomposed into any number of subdomains filled with the individual phases. In any subdomain the usual Navier-Stokes equation holds. On the interfaces, between the domains, we need to take special care. The connection between the domains is mostly based on mass and momentum conservation, although in one case, tangential velocity, physical insight and experimental facts also plays a role.

2.5.1 Mass conservation and velocity conditions

The normal velocity is related to the fluid velocity field $\mathbf{u}$ in various ways. In the simplest case, without phase change, one assumes continuity of fluid velocity

$$\mathbf{u}_1 = \mathbf{u}_2. \tag{37}$$

In general x_i denotes the limiting values of a variable x when the interface is approached from phase i. This may be written in *jump notation*, i. e. the notation $[x] = x_2 - x_1$:

$$[\mathbf{u}]_S = 0. \tag{38}$$

The interface velocity is then the normal velocity, the same on both sides of the interface:

$$V = \mathbf{u}_1 \cdot \mathbf{n} = \mathbf{u}_2 \cdot \mathbf{n}. \tag{39}$$

In the case of evaporation or more generally phase change, there may be a mass flow q from phase 1 to phase 2. This mass flow is connected to the velocities on both sides of the interface in the following way. Consider the frame of reference where the interface is at rest. The normal velocities in that frame of reference are $u' = \mathbf{u} \cdot \mathbf{n} - V$. The mass flow is the amount of mass that goes from phase 1 to phase 2, and it must the same on both sides of the interface by conservation of mass (This is simply the Rankine-Hugoniot condition):

$$\rho_1 u_1' = \rho_2 u_2' = q. \tag{40}$$

Then, in the general frame of reference

$$\rho_1(\mathbf{u}_1 \cdot \mathbf{n} - V) = \rho_2(\mathbf{u}_2 \cdot \mathbf{n} - V) = q\,. \tag{41}$$

Thus if there is no phase change, i.e. $q = 0$, one recovers eq. (39) which now appears clearly to be a consequence of mass conservation. The continuity of tangential velocities ($\mathbf{u}_t = \mathbf{u} - (\mathbf{u} \cdot \mathbf{n})\mathbf{n}$), on the other hand, is a physical assumption akin to the assumption that the slip velocity on a solid wall vanishes.

2.5.2 Momentum conservation and surface tension

Momentum conservation accross the interface also takes the form of a jump condition.

$$[-p\mathbf{1} + 2\mu\mathbf{D}]_S \cdot \mathbf{n} = \sigma\kappa\mathbf{n} + \nabla_S\sigma. \tag{42}$$

This condition may be split into a normal and tangential stress condition. In three dimensions

$$[-p + 2\mu\mathbf{n} \cdot \mathbf{D} \cdot \mathbf{n}]_S = \sigma\kappa, \tag{43}$$

$$\left[\mu\mathbf{t}^{(k)} \cdot \mathbf{D} \cdot \mathbf{n}\right]_S = \mathbf{t}^{(k)} \cdot \nabla_S\sigma, \tag{44}$$

where the vectors $\mathbf{t}^{(k)}$ are two independent tangent vectors.

2.6 Navier-Stokes equation: whole-domain formulation

In contrast to the previous approach, it is possible to express the dynamical law without resorting to jump conditions. Then the resulting differential equations are valid in the whole domain occupied by the various phases. The whole domain equation contains several singular term which balance each other. The condition that the singular terms balace is equivalent to the jump condition. It is intreresting to consider a simple one dimensional example. Consider the 1D mass conservation equation in the presence of a source of mass q at point $\mathbf{x}_s$. We thus relax the conservation of mass by allowing a source, for the purpose of the example. We have

$$\partial_t\rho + \partial_x(\rho u) = q\delta(x - x_s) \tag{45}$$

A jump of ρU must appear at point x_s to compensate the point source

$$[\rho u] = q. \tag{46}$$

The formulation with the singular source (45) is thus equivalent to the formulation with the jump condition.

Applying this to mass conservation, since there is no source term in the real world, there is also no jump as seen above and the continuity equation is valid in the whole domain:

$$\nabla \cdot \mathbf{u} = 0. \tag{47}$$

The momentum balance is modeled by the Navier-Stokes equation

$$\rho\left(\partial_t \mathbf{u} + \mathbf{u}\cdot\nabla\mathbf{u}\right) = -\nabla p + \nabla\cdot(2\mu\mathbf{D}) + \mathbf{f} + \mathbf{f}_{cap}, \tag{48}$$

where the singular force $\mathbf{f}_{cap} = \sigma\kappa\delta_S\mathbf{n} + (\nabla_S\sigma)\delta_S$ appears in addition to the other bulk forces $\mathbf{f}$. Singularities may or do appear in the terms ∇p, $\nabla\cdot(2\mu\mathbf{D})$ and $\mathbf{f}_{cap}$ of the equations, and are balanced through the jump condition on stress (42). Because of these singularities, equations (48) differs from the previous formulation of the Navier-Stokes equations (1). In particular, even if the viscosity is constant in each phase, the viscosity coefficient μ cannot be placed outside the gradient operator.

2.7 Conservative form of the surface tension forces

We may also rewrite the Navier-Stokes equation as a set of conservation laws. Conservation of momentum is then obvious. In particular, capillary effects may be represented by a tensor $\mathbf{T}$. This tensor is tangent to the interface and it is given by

$$\mathbf{T} = -\sigma(\mathbf{1} - \mathbf{n}\otimes\mathbf{n})\delta_S, \tag{49}$$

where $\mathbf{1}$ is the Kronecker symbol tensor δ_{ij}.

One may show that the capillary force may be written (Appendix)

$$\sigma\kappa\mathbf{n}\delta_S + \nabla_S\sigma\delta_S = -\nabla\cdot\mathbf{T}\,, \tag{50}$$

and then obtain an equation equivalent to (48) but in conservative form

$$\partial_t(\rho\mathbf{u}) = -\nabla\cdot\left(p\mathbf{1} + \rho\mathbf{u}\otimes\mathbf{u} + \mathbf{T} - 2\mu\mathbf{D}\right). \tag{51}$$

2.8 Problems with reconnecting interfaces

When two interfaces reconnect and change topology, as in figures 8 and 9, the above model becomes singular. Indeed, immediately after reconnection the surface is not any more a smooth surface, but it has cusp-like singularities.

The curvature κ is then ill-defined and arbitrary large in the instants immediately following reconnection. Another difficulty arises in the case represented on Fig. 9. In that case it is reasonable to assume that the velocity field is hyperbolic near the reconnection point. The interfaces then approach each other exponentially, and their separation $d(t)$ varies as $d_0\exp(-\lambda t)$ where λ is the largest eigenvalue of the rate-of-strain tensor $\mathbf{D}$ of the local velocity field. It is obvious that the separation $d(t)$ rapidly reaches scales much

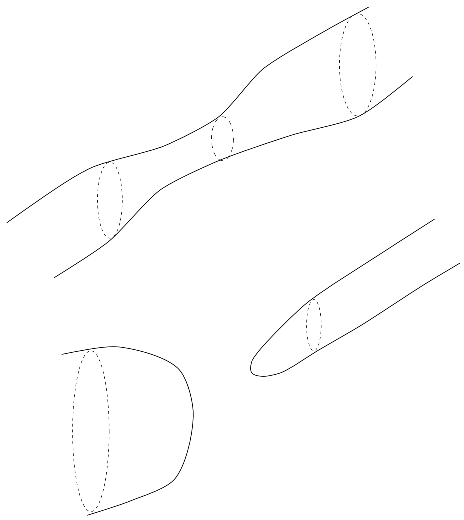

Figure 8: Interface reconnection through filament breakup. This kind of reconnection is accelerated by capillary tension. The Navier-Stokes equation predicts it will happen in finite time.

smaller than the scales on which *microscopic* molecular forces act to attract or repel interfaces (de Gennes, 1985). The exact nature of these forces depends on the fluids and on the presence of surfactants. As a rule of thumb, they must be considered prevalent on scales of 10-40 nanometers (nm).

This difficulty is less important, from the numerical point of view at least, in the case of the filamentary reconnection (Fig. 8). Indeed in that case the macroscopic impact of microscopic physics may be limited. In other words, the macroscopic interface motion may be relatively less dependent on interface physics. This is because universal macroscopic solutions that lead to a singularity in finite time may be found (Eggers, 1997). The nature of this universal singularity does not depend on the large scale flow around the singularity nor on microscopic properties (Eggers, 1993; Stone, 1994). One may then hope to solve the problem on a sufficiently fine scale to capture the singularity, just as one captures a shock in computational aerodynamics.

2.9 Free-surface flow

Free-surface flow is a limiting case of flow with interfaces, in which the treatment of one of the phases is simplified. For instance, for some cases of air-water flow, we may consider the pressure p in the air to depend only on time and not on space (through, say, some function $p_{\mathrm{air}}(t)$) and the viscous stresses in the air to be negligible. The whole-domain forms, eq. (48) or (51),

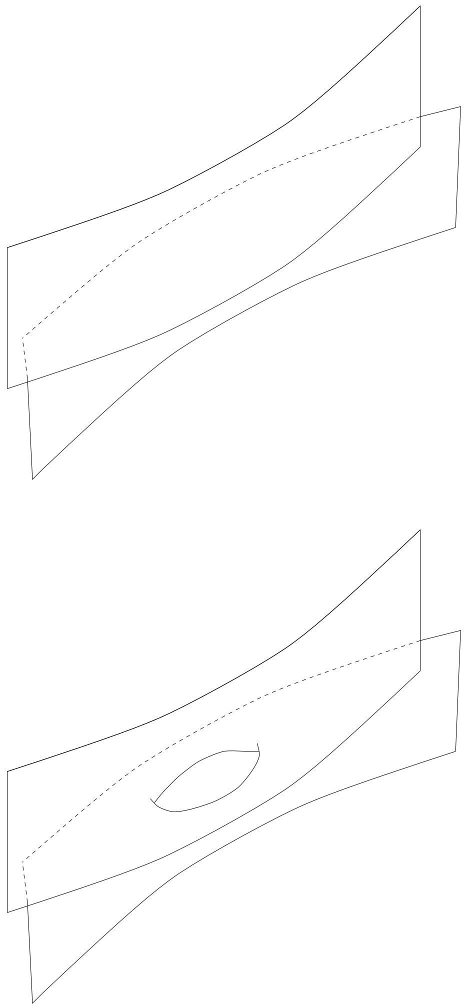

Figure 9: Interface reconnection through sheet breakup. This reconnection may occur in a hyperbolic region of the flow, in two dimensional as well as in three-dimensional flow. The computation of the final phase of reconnection requires the estimation of microscopic forces.

are then not available anymore and the bulk form without surface tension forces (2.3) must be used. The jump conditions become *boundary conditions* on the border of the liquid domain:

$$(-p + 2\mu \mathbf{n} \cdot \mathbf{D} \cdot \mathbf{n})|_S = p_{\text{air}} + \sigma\kappa \tag{52}$$

and

$$\mu\, \mathbf{t}^{(k)} \cdot \mathbf{D} \cdot \mathbf{n}\Big|_S = \mathbf{t}^{(k)} \cdot \nabla_S \sigma. \tag{53}$$

In the case of constant σ, the tangential stresses vanish and

$$\mathbf{t}^{(k)} \cdot \mathbf{D} \cdot \mathbf{n}\Big|_S = 0. \tag{54}$$

It may be noted that the last condition, which results from the nullity of tangential stresses, is purely kinematic: it does not involve material properties at all. For this reason it has interesting consequences on the value of the vorticity on a free surface (Batchelor, 1970; Longuet-Higgins, 1998).

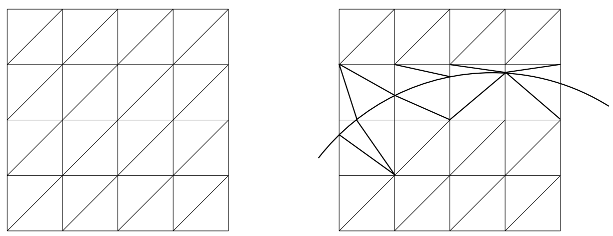

Figure 10: An example of local adaptation on an otherwise fixed grid. On the left, the undeformed finite element triangular grid. On the right, the thick line representing the interface is made up of sides of the new triangles.

3 Fixed-grid methods

In fixed-grid methods the grid used to solve the Navier-Stokes equation is entirely or quasi-entirely fixed. The grid may be quasi-entirely fixed when, for example, it is adaptive just for those cells cut by the interface, as on Fig. 10 (Glimm et al., 1986; Glimm et al., 1987).

3.1 Marker methods

In *marker-methods*, tracers or marker particles are used in the algorithm to locate the phases. Interfacial or surface-marker methods use marker particles only on the interfaces. Volume-marker methods have marker particles in the whole domain.

For two-phase flow, surface markers are more accurate than volume markers, because they track exactly the location of the interface. However, when there are more than two phases, it may become difficult to handle the complexity of triple lines (lines in three-dimensional space where three phases meet) and other effects associated with the presence of several phases. Volume markers then afford a simple way of dealing with the problem. However, an additional difficulty is that volume markers become distorted as time goes by and may need remeshing

An illustration of the surface marker method, in two particular cases, is shown on Figs. 11 and 12. One advantage of the use of surface markers is that is allows to form very thin liquid bridges that do no break, as shown on Fig. 11. However this is a real gain only in some cases. The situation may be made quite clear by considering the spiraling wave of Fig. 12. If both phases have the same viscosity and density and there is no surface tension, the interface is “transparent” to the fluid: the fluid, in a way, does not know that there is an interface. The phases are only distinguished by their “color”

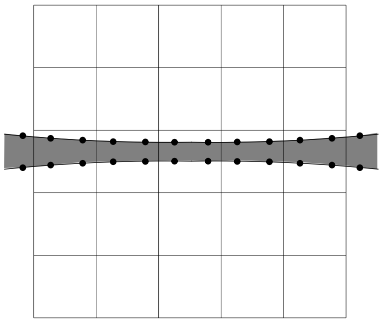

Figure 11: An example of the use of surface markers on an underlying square grid. The use of surface markers allows to maintain the thin layer shown on the figure. In other types of fixed-grid methods, this layer may break.

as an ideal passive scalar with zero diffusivity. In that case it makes sense to track details smaller than the grid.

On the other hand, if there is for instance a difference in density, there will be scales in the velocity and pressure fields much smaller than the grid, and these scales will not be well resolved using the uniform square grid of Fig. 12.

Surface marker methods have been used extensively by the Glimm group (Glimm et al., 1986; Glimm et al., 1987) and by the Tryggvason group (Tryggvason and Unverdi, 1990; Unverdi and Tryggvason, 1992a; Unverdi and Tryggvason, 1992b). Marker methods have other advantages, and an important one is the high degree of accuracy that may be achieved by representing the interface through high-order interpolation polynomials. This accuracy may allow to improve the accuracy of surface tension calculations (Popinet and Zaleski, 1999; Popinet and Zaleski, 1998).

3.2 Volume of Fluid methods

As stated in the introduction, we consider in some detail VOF methods relatively to two-dimensional incompressible flows, without mass transfer. Extension to compressible fluids can be found(Miller and Puckett, 1996), (Puckett and Saltzman, 1992). Fluxes are defined on cell faces of a square mesh with constant grid spacing $h = \Delta x = \Delta y$. The generalization to three-dimensional domains and to non-uniform rectangular and parallelepipedic grids can be done with some extra conceptual effort, but it would complicate unnecessarily this presentation(Popinet et al., 1997).

A discrete analog of the characteristic function H used in eq. (33) is the scalar field C_{ij}, known as volume fraction or color function (it actually should

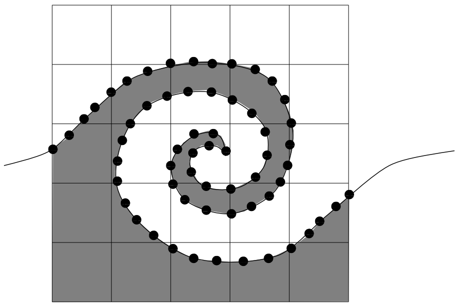

Figure 12: Another example of the use of surface markers: a vortical structure entrains the interface in a spiraling motion. Surface markers allow the capture of details of interface motion on scales much smaller than the grid spacing. However, as explained in the text, some small scale detail of the hydrodynamics may be lost when scales much smaller than the grid are created.

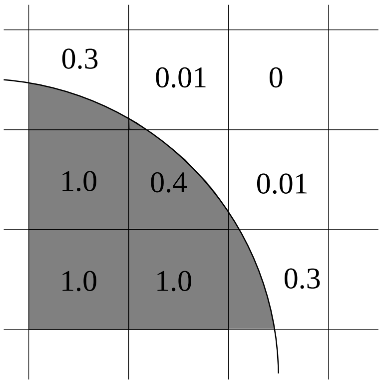

Figure 13: The exact VOF color function for a smooth circular arc over a square grid.

be area fraction in two dimensions, but the standard appellation is volume fraction). The color function $C_{i,j}$ represents the portion of the area of the cell (i, j) filled with phase 1:

$$C_{ij}h^2 \approx \int\int_{(i,j)} H(x, y)\ dx\, dy.$$

We have $0 < C < 1$ in cells cut by the interface S and $C = 0$ or 1 away from it. An example of a color function corresponding to a circle arc is shown on Fig. 13. In an incompressible flow, mass conservation is equivalent to conservation of volume and hence of the characteristic function H. There is a vast literature of numerical methods for conservation laws, however an explicit account needs to be taken of the special nature of the problem, which is entirely concentrated on the interface S. Moreover, particular care has to be given to the constraint $0 < C < 1$, because numerical errors in the estimation of the fluxes can lead to values of C outside the physical range of validity.

VOF methods have been known for several decades and have been gone through a continuous process of improvement. Their large use and effectiveness is due to several reasons:

1. They preserve mass in a natural way, as a direct consequence of the development of an advection algorithm based on a discrete representation of the conservation law (33).

2. No special provision is necessary to perform reconnection or breakup of the interface and in this sense the change of topology is implicit in the algorithm.

3. They can be relatively simply extended from two-dimensional to three-dimensional domains.

4. The scheme is local in the sense that only the C values of the neighboring cells are needed to update the C value in the cell (i, j). For this reason, it is relatively simple to implement these algorithms in parallel, in particular within the framework of domain decomposition techniques.

In general, a VOF algorithm solves the problem of updating the volume fraction field C given the fixed grid, the velocity field $\mathbf{u}$ and the field C at the previous step. In two dimensions, the interface is considered to be a continuous, piecewise smooth line and the problem of its reconstruction is that of finding an approximation to the section of the interface in each cut

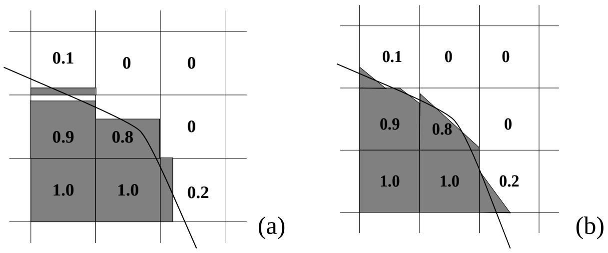

Figure 14: Two attempts at interface reconstruction (a) First-order or SLIC and (b) second-order, or PLIC.

cell, by knowing only the volume fraction C in that cell and in the neighboring ones. The simplest types of VOF-methods are the Simple Line Interface Calculation (SLIC) of ref. (Noh and Woodward, 1976) or the SOLA-VOF algorithm of (Hirt and Nicholls, 1981). They are first order, $\mathcal{O}(h)$, in the accuracy of the reconstruction of the interface. Typically, the reconstructed interface is made up of a sequence of segments aligned with the grid, as shown in Fig. 14a. The reconstruction is relatively crude, and its advection even with simple velocity fields, such as translations or solid body rotations, generates a large number of floatsam. A few improvements have been made by several authors (Chorin, 1980), (Lafaurie et al., 1994), but these features still remain.

More accurate VOF techniques attempt to fit the interface through piecewise linear segments. This was already implemented in some of the earliest VOF methods (DeBar, 1974). The more accurate techniques are now known as the Piecewise Linear Interface Construction (PLIC) method (Ashgriz and Poo, 1991),(Li, 1995),(Parker and Youngs, 1992), (Rider and Kothe, 1995),(Pilliod Jr and Puckett, 1997),(Gueyffier et al., 1999).

To understand the reconstruction problem we have represented in each cell of Fig. 15a,b a possible distribution of the color function on the square grid. In case (b), it is harder to determine the location of the interface, but a robust reconstruction method must be able to handle this case too without any ambiguity.

One of the critical simplifying features of VOF/PLIC algorithms is that one does not attempt to reconstruct the interface as a chain of *joined* segments (a continuous chain of segments), but as a discontinuous chain with however asymptotically small discontinuities.

Whenever the curvature is small (i.e. the radius of curvature is large with respect to the grid size) the method will be accurate. However, it is *robust* in the sense that it does not have a catastrophic behavior when the curvature increases or even becomes infinite, for instance at reconnection. Specifically,

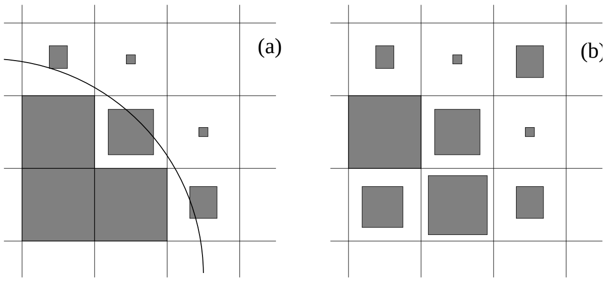

Figure 15: Representing the color function as shaded squares of size proportional to the fractional volumes may help to understand the reconstruction problem: (a) shows a well-behaved distribution of the color function. It corresponds to a smooth circular arc; (b) shows a more confused distribution.

when the curvature is small, the jumps in interface position at discontinuities are of order $||[\mathbf{x}]|| \simeq \mathcal{O}(\kappa h^2)$. When the curvature is large, we lose all details at scales smaller than the grid size h.

A VOF/PLIC algorithm is divided in two parts: a reconstruction step and a propagation step. (This splitting also occurs in the numerical resolution of conservation laws.) We now describe these two components.

3.2.1 Reconstruction

The key part of the reconstruction step is the determination of the orientation of the segment. This is equivalent to the determination of the unit normal vector $\mathbf{n}$ to the segment. Then, the normal vector $\mathbf{n}$ and the volume fraction C uniquely determine the straight line.

A typical reconstruction is shown in Fig. 14b. Several algorithms have been developed for the calculation of the normal vector (Puckett and Saltzman, 1992),(Parker and Youngs, 1992). Here, we briefly review two of them. In the first one (Li, 1995), a normal (non-unit) vector $\mathbf{m}$ is estimated by a finite-difference formula:

$$\mathbf{m}^h = \nabla^h C. \tag{55}$$

This vector $\mathbf{m}$ is cell-centered and it is approximated by first evaluating the cell-corner values of $\mathbf{m}$, for example at position $(i+1/2, j+1/2)$:

$$m_{x,i+1/2,j+1/2} = \frac{1}{2h}\left(C_{i+1,j} - C_{i,j} + C_{i+1,j+1} - C_{i,j+1}\right) \tag{56}$$

$$m_{y,i+1/2,j+1/2} = \frac{1}{2h}\left(C_{i,j+1} - C_{i,j} + C_{i+1,j+1} - C_{i+1,j}\right) \tag{57}$$

The required cell-centered value is obtained by averaging:

$$\mathbf{m}_{ij} = \frac{1}{4}(\mathbf{m}_{i+1/2,j-1/2} + \mathbf{m}_{i-1/2,j-1/2} + \mathbf{m}_{i+1/2,j+1/2} + \mathbf{m}_{i-1/2,j+1/2}). \quad (58)$$

This estimation of the normal is sometimes called the Parker and Youngs approach (PY). In two dimensions, the discrete gradient $\nabla^h C$ is constructed from the volume fraction values of a 3×3 block of cells centered at (i, j).

An alternate approach is a least-square method (Puckett, 1991). The same block of cells is considered, but now the interface is approximated by a straight line in the whole block, with the constraint that the volume fraction of the central cell is always the true value C. By changing the slope of the line, one can minimize the discrete error between the true values C and the values $\tilde{C}$ given by the linear approximation. For example, the discrete error E in L^2 norm at cell (i, j) is given by the expression:

$$E(\mathbf{m}) = (\sum_{k,l=-1}^{1} (\tilde{C}_{i+k,j+l}(\mathbf{m}) - C_{i+k,j+l})^2)^{\frac{1}{2}}. \quad (59)$$

More recently, the "ELVIRA" approach was proposed (Pilliod Jr and Puckett, 1997). In ELVIRA the slope is chosen among six "candidates" given by the backward, central and forward differences of the column sums of the volume fractions done along the x and the y directions, respectively. The candidate that yields the lowest value of the error in (59) wins.

The ELVIRA approach reconstructs exactly (within machine precision) a straight line interface. This method is thus truly second order, $\mathcal{O}(h^2)$, unlike (PY), which is intermediate between first and second order (Pilliod Jr and Puckett, 1997). Numerical experiments show however that at *low to medium resolution* it does not always give better results than (PY), but as the resolution increases, ELVIRA gives the best results, as it should be expected. This typically occurs when there are more than 20 grid points along the bubble diameter.

In the second part of the reconstruction, a linear interface which divides the computational cell into two parts containing the proper area of each fluid must be found. In general, the "forward" problem of finding the area within a square on each side of a given linear interface is more straightforward than the "inverse" problem of obtaining the equation for the linear interface, given the fraction of area contained on each side and the normal direction. Both are needed in the reconstruction and propagation steps of PLIC. We achieve this by deriving an explicit expression which relates the "cut" area to a parameter α which fully defines the straight line (Gueyffier et al., 1999).

In two dimensions, the problem can be stated as follows. Given a square cell of side h in the (x, y) plane and a straight line (such as EH on Fig. 16)

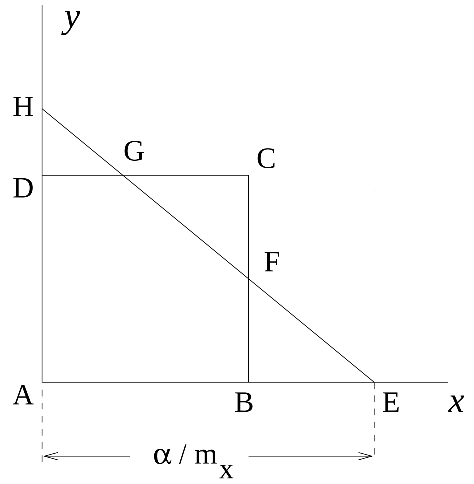

Figure 16: Geometrical basis for expression (61).

with normal vector $\mathbf{m}$, find the area of the region below the line which also lies within the square cell. This corresponds to the area $ABFGD$ on Fig. 16. To obtain an expression for this area, let us suppose that the components m_x and m_y of the normal are both positive (this can always be arranged by a simple coordinate transformation); in case one of the components vanishes, the calculation of the area becomes trivial. The most general equation for a straight line in the (x, y) plane with normal $\mathbf{m}$ is

$$m_x x + m_y y = \alpha \,, \tag{60}$$

where α is a parameter. The area of the region contained below this line within the square cell (i, j) ($ABCD$ of Fig. 16) is given by

$$\begin{aligned} \text{Figures}/C_{ij} \quad &= \quad \frac{\alpha^2}{2m_x m_y} \left[1 - H(\alpha - m_x h) \left(\frac{\alpha - m_x h}{\alpha} \right)^2 \right. \\ &\qquad \left. - H(\alpha - m_y h) \left(\frac{\alpha - m_y h}{\alpha} \right)^2 \right] \,. \end{aligned} \tag{61}$$

The prefactor $\alpha^2/2m_x m_y$ on the right-hand side of this equation is simply the area of the triangle AEH. In case points E and H lie within the original square, this is the desired area. When $\alpha > m_x h$, point E is to the right of point B and we must subtract the area of the small triangle BEF to obtain the proper area. Since triangle BEF is geometrically similar to triangle AEH, the ratio of their areas is equal to the square of the ratio of the sides

BE to AE, given by

$$\frac{\text{Figures/Area of } BEF}{\text{Figures/Area of } AEH} = \left(\frac{\alpha - m_x h}{\alpha}\right)^2 .$$

This corresponds to the second term within the square brackets on the right-hand side of (61), which also contains the Heaviside step function $H(\alpha - m_x h)$, since the area of the triangle BEF is only subtracted if E is to the right of B. Similarly, the third term within the square brackets in (61) subtracts the area of the triangle DGH when $\alpha > m_y h$ and point H lies above point D. The single formula (61) thus provides the area of the region below the straight line (60) which lies in the original square of side h for all possible cases. The area is a continuous, one-to-one, monotonically increasing function of α. It ranges from zero, when $\alpha = 0$, to h^2, when α reaches its maximum value of $(m_x + m_y)h$. There are two critical values of α, corresponding to the zeros of the arguments of the Heaviside step functions in (61), at which the function changes form. This occurs when the straight line (60) passes through the corners B and D of the square, i.e. when $\alpha = m_x h$ or $\alpha = m_y h$.

In practice, not only does one need the "forward" relation (61) between the cut area and the parameter α, but the method also requires the "inverse" problem of determining the α which corresponds to a given cut area and normal direction in a computational cell. There are a number of ways to achieve this. One can simply use a standard root-finding approach to find the particular value of α at which the cut area has the desired value. Another option is as follows: corresponding to each critical value of α for which the interface passes through one of the corners of the square, there exists a critical value of the cut area. In between any two critical values, the function (61) is a known polynomial in α whose roots can be evaluated analytically. Thus, to resolve the inverse problem, we first identify which two critical values bound it on either side, and then obtain the root of the correct polynomial in α in that range.

3.2.2 Propagation

The second step of the VOF algorithm is propagation. Once the interface has been reconstructed, its motion by the underlying flow field must be modeled by a suitable advection algorithm. Here, we describe in some detail the fractional step or operator split method, which updates the volume fraction C by advecting the interface along one spatial direction at a time. Intermediate C values are calculated during this process, and the final C field is obtained only after advection of the interface along all coordinate directions.

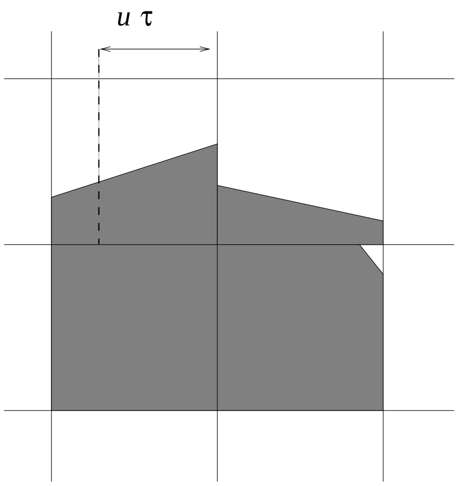

Figure 17: A simple scheme for the split computation of the fluxes: as in the upwind differencing scheme, the whole block of fractional volume in a band of width $u\tau$ is transferred from the upwind cell to the downwind cell. No account however is taken of the change of shape of the interface during the time step.

One oft-used way to calculate fluxes along the x direction is shown in Fig. 17, where all the fluid to the right of the dashed line will cross the right boundary during time τ. In our calculations (Gueyffier et al., 1999) we use a Lagrangian approach, that is, we compute directly the motion of the interface segments. We have found this scheme to be more robust. Since in practice, the time-stepping is performed separately in each spatial direction, we will only describe the advection of the interface along one spatial coordinate, say x.

For each cell, three contributions are calculated: the area fluxes ϕ^- and ϕ^+ entering the cell (i,j) respectively from cells $(i-1,j)$ and $(i+1,j)$ and the area ϕ^0 of the fluid contained at the beginning of the step in the control cell which remains there. The updated volume fraction in each cell after the fractional step along the x direction is then given by

$$C_{i,j}^{(x)} = \left[\phi_{i,j}^- + \phi_{i,j}^0 + \phi_{i,j}^+\right] . \tag{62}$$

Then, the overall fractional-step procedure requires two reconstructions of the interface and an advection step along each one of the two coordinate directions. The Lagrangian advection method allows us to take into account the stretching or compression of the interface during each single fractional step. The procedure can be made second-order accurate by alternating the advection directions at each time step.

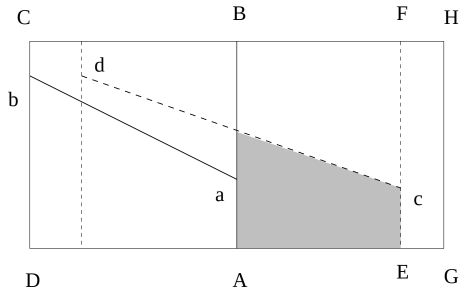

Figure 18: A Lagrangian propagation step. The advection of the reconstructed segment is computed, defining a new segment that straddles two cells. From that new segment, fluxes are calculated.

Unsplit algorithms are geometrically more complex, because they also need to take into account fluxes along the transverse direction, for example from cell (i, j) to cell $(i+1, j+1)$. First-order and second-order accurate algorithms have been developed by several authors (Collela, 1990), (Bell et al., 1990), (LeVeque, 1996),(Puckett et al., 1997). The results they present indicate that for a given order of accuracy of the advection model, the unsplit algorithm shows better resolution, especially near regions of high variation of the derivatives, such as corners.

3.3 Tridimensional VOF

This method can be generalized to three dimensions with little conceptual difficulty. For this purpose, consider the schematic drawing in fig. 19 of the right parallelepiped $ABCDEFGH$ of sides $AH = c_1$, $AB = c_2$ and $AD = c_3$, which is intersected by the planar surface IJK. If the normal to this surface is denoted by $\mathbf{m}$, all points which lie on it satisfy the equation

$$m_1x_1 + m_2x_2 + m_3x_3 = \alpha\,, \tag{63}$$

in which, as before, we take the components m_1, m_2 and m_3 of the normal to be positive. We also have that $AI = \alpha/m_1$, $AJ = \alpha/m_2$ and $AK = \alpha/m_3$. To find the volume of the region below this interface contained in the original parallelepiped, i.e. the volume $ABGHLMNK$, we begin with the volume of the large tetrahedron $AIJK$, which is given by

$$\frac{\alpha^3}{6m_1m_2m_3}\,,$$

and subtract the volumes of the tetrahedra which protrude outside of the original parallelepiped. In fig. 19, these correspond to the volumes $HIPL$

and $BOJN$. Each of these tetrahedra is geometrically similar to the original one, and the ratio of their volumes to that of $AIJK$ is given respectively by $(1 - m_1c_1/\alpha)^3$ and $(1 - m_2c_2/\alpha)^3$. However, since the volume of the small tetrahedron $GOPM$ would then be subtracted twice, we would have to add that volume to the resulting expression, provided that the line IJ lies outside the rectangle $ABGH$ in the first place; that is, provided that $\alpha > (m_1c_1 + m_2c_2)$. The ratio of the volume of the small tetrahedron $GOPM$ to that of the large tetrahedron $AIJK$ can be found, using geometric similarity, to be $(1 - m_1c_1/\alpha - m_2c_2/\alpha)^3$. Upon combining these results and accounting for the fact that point K may also at times move above point D, the expression for the volume of interest turns out to be:

$$\begin{aligned} \text{Figures/Volume} \;=\; & \frac{1}{6m_1m_2m_3}\,[\,\alpha^3 \\ & -\sum_{j=1}^{3} H(\alpha - m_jc_j)(\alpha - m_jc_j)^3 \\ & +\sum_{j=1}^{3} H(\alpha - \alpha_{\text{Figures/max}} + m_jc_j)(\alpha - \alpha_{\text{Figures/max}} + m_jc_j)^3\,] \end{aligned} \tag{64}$$

in which

$$\alpha_{\text{Figures/max}} = m_1c_1 + m_2c_2 + m_3c_3\,.$$

In (64), the second line achieves the subtraction of the volumes of the tetrahedra which protrude from the faces of the original right parallelepiped, in case points I, J and K move beyond points H, B and D, respectively. And the third lines adds back the volumes of the small tetrahedra like $GOPM$, in case the lines IJ, JK and KI lie outside the rectangular faces $ABGH$, $ABCD$ and $ADEH$, respectively.

Equation (64) provides a continuous, one-to-one, monotonically increasing, functional relation between the volume inside a right parallelepiped lying below the planar interface (63) and the parameter α which fully characterizes the plane.

In practice, not only does one need the "forward" relation (64) between the cut volume and the parameter α, but the method also requires the "inverse" problem of determining the α which corresponds to a given cut volume and normal direction in a computational cell. There are a number of ways to achieve this. One can simply use a standard root-finding approach, such as Bisection or Newton's Method (note that the derivative of the right-hand side of (64) with respect to α can be calculated readily) to find the particular value of α at which the cut volume has the desired value. Another iterative method to determine α is presented in (Rider and Kothe, 1998). Another

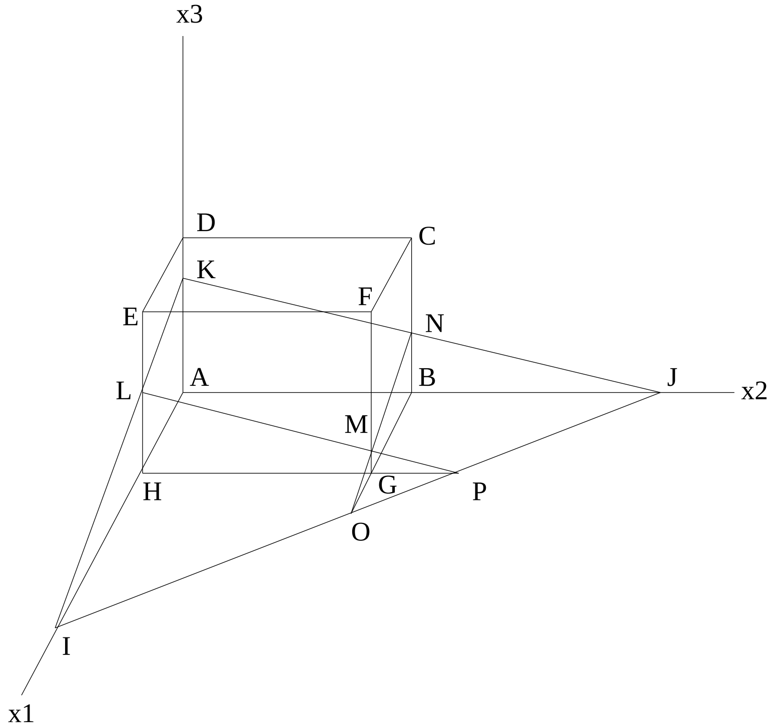

Figure 19: The “cut volume” refers to the region contained within the right parallalepiped $ABCDEFGH$ and also below the planar surface IJK, which has normal $\mathbf{m}$ and parameter α.

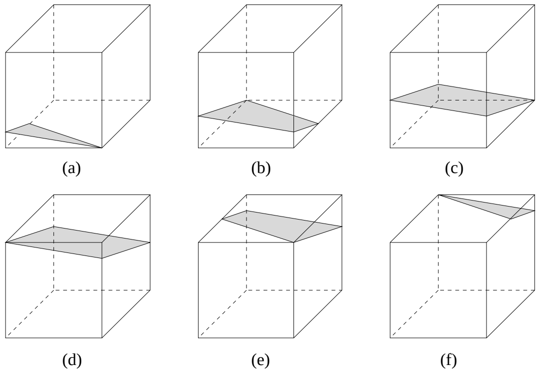

Figure 20: The different critical shapes of the cut cube for $m_1 + m_2 < m_3$. The cut cube changes shape each time the plane crosses a vertex. Each shape corresponds to a specific critical volume and a corresponding critical α. In between each critical pair, the cut volume is a cubic polynomial in α.

option, which is the one we have actually implemented, is as follows: Corresponding to each critical value of α for which the interface passes through one of the corners of the cube, there exists a critical value of the cut volume. In between any two critical values, the function (64) is a cubic polynomial in α whose roots can be evaluated analytically. Thus, to resolve the inverse problem, given the desired cut volume, we first identify which two critical values bound it on either side, and then obtain the root of the correct cubic polynomial in α in that range.

In this instance, in order to simplify the search for the critical bounds, it is better to number the coordinates such that the order in which the various corners are crossed is (almost) pre-determined. On a unit cube with all sides equal to unity, for instance, we can number the coordinates so that $0 < m_1 < m_2 < m_3$. In that case, the order in which the corners of the cube are crossed as α increases depends only upon whether $m_1 + m_2$ is smaller or larger than m_3. Figures 20 and 21 represent the six critical shapes of the cut cube in each of the two possible cases.

More recently, it has been shown (Pilliod Jr and Puckett, 1997) that the minimizing slope is one among six candidates given by the backward, center and forward differences of the column sums of the volume fractions done along the x and the y directions, respectively. The candidate that yields the lowest value of the error in (59) wins. This algorithm is known as Efficient Least Squares Volume-of-Fluid Interface Reconstruction Algorithm (ELVIRA).

These two VOF/PLIC algorithms suffer of several simplifying features: the reconstructed interface is given by a sequence of discontinuous segments, with however asymptotically small discontinuities, and the local curvature

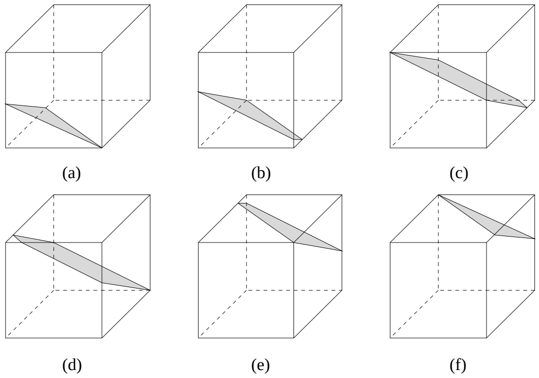

Figure 21: The different shapes of the cut cube for $m_1 + m_2 > m_3$. The cut cube changes shape each time the plane crosses a vertex. The cubic equation relating the cut volume and α depends on the placement of the plane between the six critical positions depicted here.

can only be inferred by looking at the reconstruction in neighboring cells.

3.4 VOF with circle-fitting

Recently, R. Scardovelli proposed a new method that is able to partially overcome these problems. We start from the ELVIRA reconstruction in the 3×3 block of cells centered at cell (i, j). We then minimize the functional:

$$\sum_i (x_i^2 + y_i^2 + a\,x_i + b\,y_i + c) \quad (65)$$
$$(x_i^2 + y_i^2 + a\,x_i + b\,y_i + c) \geq 0\,,$$

where (x_i, y_i) are the coordinates of the end and middle points of the segments, whose number is ≥ 3. Basically we are fitting with a least-squares technique a circle to these points. We calculate the two intersections of the circle with the cell boundary and move the central point of the segment connecting the intersections in such a way to conserve the volume fraction C. As a final result, the interface in each cell is defined by the two segments connecting the intersections with the central point. This representation gives an estimate, even if rough, of the local curvature and moreover the discontinuities at the cell boundary are greatly reduced. We also point out that when this reconstruction is not successful, we maintain the single line reconstruction.

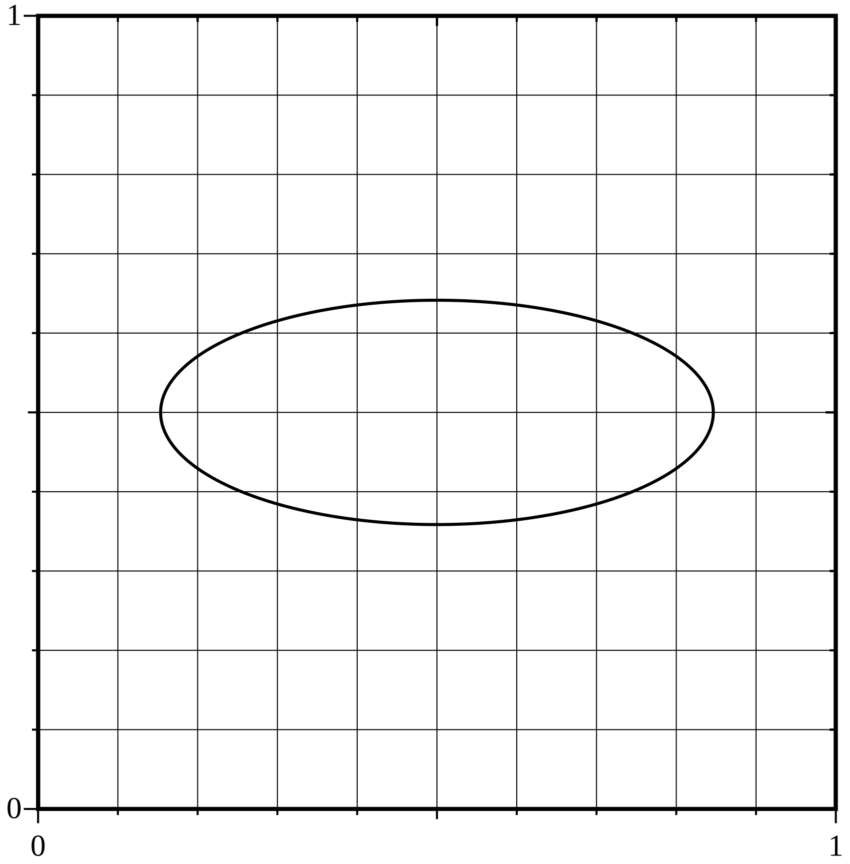

Figure 22: Initial ellipse and coarsest mesh

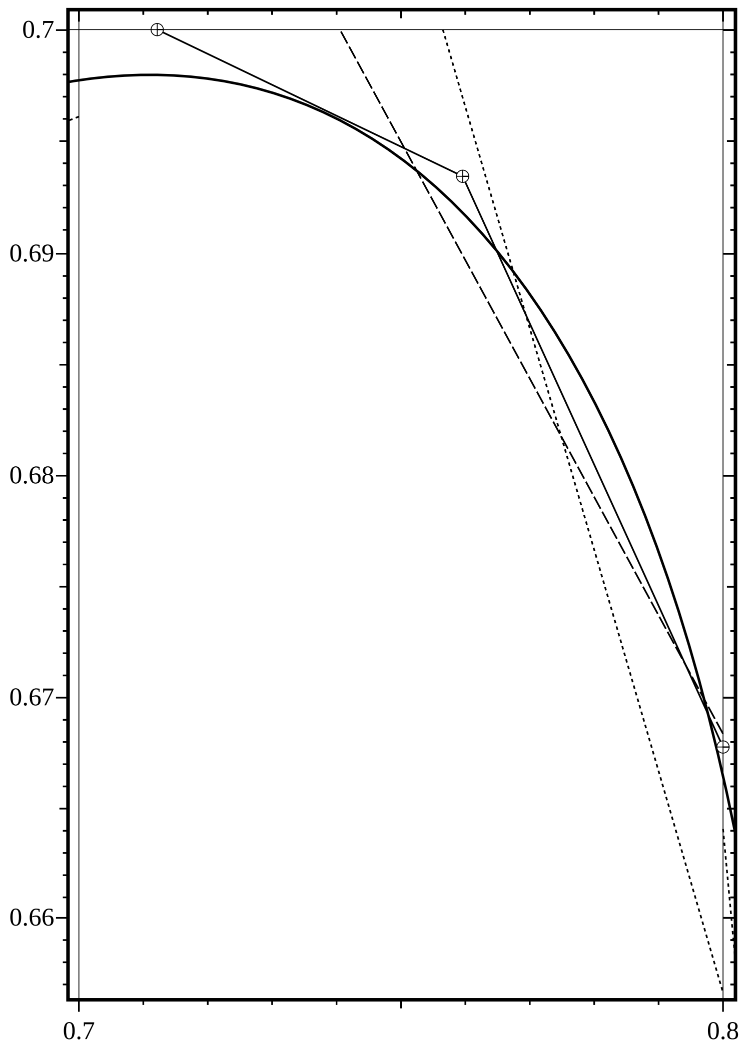

Figure 23: Reconstructions in a cell of the coarsest mesh. The thick solid line is the real line, the dotted line is the CIAM reconstruction, the dashed line the ELVIRA reconstruction, while the thin solid lines with circles at the end points is the one given by our new method

	CIAM	ELVIRA	New
grid	error/**order**	error/**order**	error/**order**
10^2	3.86e-3	4.78e-3	3.66e-3
	2.31	**2.43**	**2.73**
20^2	7.78e-4	8.86e-4	5.50e-4
	1.81	**2.38**	**2.73**
40^2	2.21e-4	1.79e-4	8.30e-5
	1.40	**2.13**	**2.66**
80^2	8.40e-5	4.10e-5	1.31e-5
	1.15	**2.04**	**2.33**
160^2	3.78e-5	1.00e-5	2.61e-6
	1.06	**2.00**	**2.10**
320^2	1.81e-5	2.49e-6	6.09e-7

Table 1: L_1 ellipse reconstruction errors and convergence rates using PY normal estimation , ELVIRA and the circle fitting method

3.5 Convergence tests

In order to check the performance of the method we analyze the following test problem. In the unitary square domain we draw the ellipse: $x^2/a^2+y^2/b^2 = 1$, with $a^2 = .12$ and $b^2 = .02$ (see Fig. 22). We choose an ellipse because the curvature is continuously changing. Here the ratio between the maximum and minimum radius of curvature is about 14.697, and moreover fitting a circle with a circle is rather tautological.

We initialized the C field in each cut cell using the analytic equation of the ellipse. In Figure 23, we show the real line and the three reconstructions in a cell of the coarsest mesh. This is a not typical case, usually the three approximations are closer to each other, but it is good for a graphical representation.

We consider the L_1 norm error between the real line l_r and each different linear approximation l_{app}:

$$E_1 = \int \mid l_r(x) - l_{app}(x) \mid \, dx \tag{66}$$

To remove fluctuations we averaged (66) over 50 ellipses with randomly generated centers and angles between the major semi-axis and the horizontal coordinate line. The coarsest grid had 10^2 points and the most refined one 320^2. The results are presented in Table 1.

4 Resolution of the Navier-Stokes equations

4.1 Time marching

We note with a superscript (n) the velocity fields at time t_n, the time step is then $\tau = t_{n+1} - t_n$. The VOF/PLIC method may be symbolized as

$$C^{(n+1)} = \mathcal{L}(C^{(n)}, \mathbf{u}^{(n)}, \tau), \tag{67}$$

where the operator $\mathcal{L}$ expresses the action of the algorithm used to advance the VOF color fraction. For the time marching of the velocity field, we first compute a provisional field $\mathbf{u}^{(*,*)}$. We use the already computed $C^{(n+1)}$ field instead of $C^{(n)}$ to improve stability. For simplicity of programming we use two steps:

$$\mathbf{u}^{(*)} = \mathbf{u}^{(n)} + \tau L_v(C^{(n+1)}, \mathbf{u}^{(n)}) + \tau L_s(C^{(n+1)}) + \tau \mathbf{g} \tag{68}$$

$$\mathbf{u}^{(*,*)} = \mathbf{u}^{(*)} + \tau L_i(\mathbf{u}^{(*)}), \tag{69}$$

then we project it on the space of incompressible velocity fields. Pressure is the solution of the following Poisson problem with homogeneous Neumann boundary conditions

$$\left\{ \begin{array}{l} \nabla \cdot \left(\frac{1}{\rho} \nabla p \right) = \frac{1}{\tau} \nabla \cdot \mathbf{u}^{(*,*)} \quad \text{in } \Omega, \\ \mathbf{n} \cdot \nabla p = -\frac{\rho}{\tau} \left(\mathbf{u}^{(n+1)} - \mathbf{u}^{(*,*)} \right) \cdot \mathbf{n} = 0 \quad \text{on } \partial\Omega, \end{array} \right. \tag{70}$$

where $\mathbf{n}$ is the normal to $\partial\Omega$. The new velocity field at time step t_{n+1} is given by

$$\mathbf{u}^{(n+1)} = \mathbf{u}^{(*,*)} - \frac{\tau}{\rho} \nabla p. \tag{71}$$

If p is a solution of (70), the velocity field $\mathbf{u}^{(n+1)}$ verifies the incompressibility equation

$$\nabla \cdot \mathbf{u}^{(n+1)} = 0. \tag{72}$$

4.2 Discretization of spatial derivatives

In all expressions of the previous section, the continuous derivatives are replaced by central differences on the MAC staggered grid (Peyret and Taylor, 1983; Lafaurie et al., 1994). The expressions for these central differences are well-known and we consequently omit them here. Using an explicit in time, centered in space finite-difference scheme introduces classical limitations on the time-step and on the mesh Reynolds number which are addressed for instance in (Peyret and Taylor, 1983). The resulting discretization may also be considered to be the result of a finite-volume formulation, since we write the equations for momentum in a conservative form when $\rho_1 = \rho_2$. The finite volumes for the horizontal velocity $u_{x,i-1/2,j,k}$, for instance, are shifted by a half-grid spacing with respect to the control volumes for volume fraction C_{ijk}. In some cases, however, the estimation of the density and viscosity requires some clarification. In the method reported here, we compute μ and ρ at each node through a simple volume average over the cell:

$$\rho_{ijk} = \rho_1 C_{ijk} + \rho_2(1 - C_{ijk}), \tag{73}$$

$$\mu_{ijk} = \mu_1 C_{ijk} + \mu_2(1 - C_{ijk}). \tag{74}$$

The discretization of the term

$$\frac{1}{\rho}\nabla p \tag{75}$$

in eqs. (70) and (71) is an especially important issue, since this term may be singular for two reasons, first because the pressure p jumps across the interface (as a consequence, for instance of Laplace's law) and second because ρ also jumps. Away from cell centers, two choices are possible: (i) the simplest one is an average of the values at neighboring cells, as in

$$\rho_{i+1/2,j,k} = \frac{1}{2}(\rho_{i,j,k} + \rho_{i+1,j,k}); \tag{76}$$

(ii) alternatively, we may choose to reconstruct the interface in a shifted cell $V_{i+1/2,j,k}$ centered on $\mathbf{x}_{i+1/2,j,k}$. This reconstruction would use the segments already constructed by the PLIC method for cells V_{ijk} and $V_{i+1,j,k}$; (iii) yet another option is to smooth the jump of ρ in the same way that the jump of H is smoothed for the computation of surface tension.

A sharp interface (option (ii)) is more accurate and somewhat prevents the diffusion of density and momentum. However, there are two facts that temper this advantage: we sometimes get a slower convergence of the multigrid method that we use to invert eq. (70), and we still do not obtain second-order spatial accuracy for the solution of the pressure field (Second-order accuracy means that the error made in the computation of pressure forces is $\mathcal{O}(h^2)$. Here it is of order $\mathcal{O}(h\Delta p)$ where Δp is the pressure jump across the interface (Popinet and Zaleski, 1999)).

While we have at times used option (ii) for pressure calculations in two dimensions, we use option (i) in three dimensions and for all the off-center values of viscosity. In several instances, it is likely that option (iii) is required to smooth the discontinuity occurring at the interface for the term (75). The need for such a smoothing is strongly advocated, for instance, in (Unverdi and Tryggvason, 1992b).

4.3 Discretization of surface tension

4.3.1 Smoothing and cut-cell methods

The surface tension term in the Navier-Stokes equation creates the most obvious difficulties, since it is a singular term. In several implementations of the method, these difficulties are manifest in both numerical instabilities and/or noise, and in poor accuracy of capillary effects.

On the fixed grids we use, there are two options:

- smoothing the capillary force: surface tension is implemented in a simple, albeit approximate way, by distributing it over neighboring grid points;

- "Cut-cell" techniques: these amount to accurate finite volume balance of surface tension forces as realized in (Popinet and Zaleski, 1999). This option has been used only for two-dimensional calculations, because of the complexity of the geometrical considerations involved.

We only describe the first option in what follows.

4.3.2 Smoothing the discontinuity of capillary forces

Several articles introduce what amounts in effect to distributing the surface tension over grid points neighboring the interface. Consider the phase-characteristic function H. It may be smoothed by convolution with a kernel

$$\tilde{H}(\mathbf{x}) = \int_V H(\mathbf{x}')H(\mathbf{x}-\mathbf{x}';\epsilon)d\mathbf{x}' \,, \tag{77}$$

where $H(\mathbf{x};\epsilon)$ is an integration kernel verifying $H \to \delta_S$, when $\epsilon \to 0$. The computation is based on the following remark: for a given value of c let S_c be the surface with equation $\tilde{H}(\mathbf{x}) = c$, $\tilde{\kappa}(\mathbf{x})$ the curvature of S_c at $\mathbf{x}$ and $\mathbf{m} = \nabla\tilde{H}$. Then from (5)

$$\tilde{\kappa}(\mathbf{x}) = -\nabla\cdot\left(\frac{\mathbf{m}}{2||\mathbf{m}||}\right) . \tag{78}$$

When $\epsilon \to 0$, $\tilde{\kappa} \to \kappa$ and one finds the "real" curvature. After (Brackbill et al., 1992) this method is sometimes called the Continuous Surface Force (CSF) method. To implement the CSF method it is not necessary to perform a great deal of smoothing. Several authors from which we had private communications, as well as ourselves have implemented directly finite differences of H without smoothing or with very narrow kernels without any major problem. A discussion of the merits of better kernels may be found in (Aleinov and Puckett, 1995). In (Lafaurie et al., 1994) we defined the finite filter

$$[\mathcal{F}(C)]_{ij} = \frac{1}{2}C_{ij} + \frac{1}{8}[C_{i,j-1} + C_{i,j+1} + C_{i-1,j} + C_{i+1,j}]\,. \tag{79}$$

The action of this filter may be repeated m_f times to yield an additional degree of smoothing $\tilde{C} = \mathcal{F}^{(m_f)}(C)$. The gradient $\mathbf{m}$ is then computed by finite differences, using for instance expressions (56) and (57). We have found that one or two iterations of this filter were optimal.

4.3.3 Momentum conservation

The smoothing method allows to find an approximation of the singular tensor defined in equation (49)

$$\mathbf{T} = \sigma(\mathbf{I} - \mathbf{n} \otimes \mathbf{n})||\nabla\tilde{C}||\,, \tag{80}$$

where the unit normal $\mathbf{n}$ is

$$\mathbf{n} = \frac{\nabla\tilde{H}}{||\nabla\tilde{H}||}\,. \tag{81}$$

The momentum-conserving formulation is a finite difference approximation of (80). In practice, a 4- or 6-point approximation was used for the computation of the normals.

As in the method of ref. (Brackbill et al., 1992) this approximation converges in theory towards the true normal as $H \to \delta_S$. When the kernel H_ϵ is narrowed one should keep m_f large in order to have $h \ll \epsilon$, however numerical experiences have shown that the best results are obtained when $m_f = 1$ or 2. Larger values of m_f increase the spurious currents.

4.3.4 Capillary wave test

Since derivatives of rapidly varying functions are estimated by finite differences in the above discretization, convergence is not self-evident. Clearly, proof of the convergence of the method must lie in its ability to reproduce known flows in test cases. An example of the results obtained with the VOF/PLIC method combined with CSS is given in the case of a capillary wave over a flat interface. For a sinusoidal wave with an initial amplitude a_0 and a wavenumber k, the non-dimensional amplitude a/a_0 is a function of the non-dimensional time $\tau = \omega_0 t$ with $\omega_0^2 = \sigma k^3/(\rho_1 + \rho_2)$ and the non-dimensional viscosity $\epsilon = \nu k^2/\omega_0$.
We simulate capillary waves between two viscous fluids of equal density ρ and viscosity μ. We initialize a sinusoidal perturbation whose wavelength is equal

to the box width and let it oscillate. Free-slip conditions are imposed on top and bottom boundaries, and periodic conditions on the vertical boundaries. The relevant parameters for the test case are viscosity $\epsilon = 6.472 \times 10^{-2}$, frequency $\omega_0 = 6.778$ and Ohnesorge number Oh $= 1/\sqrt{3000}$.

We have compared the time evolution of the capillary wave amplitude with the initial-value theory of (Cortelezzi and Prosperetti, 1981; Prosperetti, 1981). The remaining error is a function of the of the grid size h and of the initial wave amplitude a_0. We have studied how varying the grid size h and the ratio h/a_0 influences the convergence toward the analytical solution. We found that the numerical solution converges toward the analytical solution of the initial-value problem. We found (Table II) that when we increased the ratio h/a_0 until it reaches about 1, the non-linear effects become less important and the numerical results converge toward the analytical solution. When h/a_0 is much larger than 1, the wave amplitude is not resolved anymore by the grid size and the numerical results diverge. For sufficiently small h, typically from 128^2 to 512^2, there appear to be convergence but at a sublinear rate. A similar slow convergence was observed in (Popinet and Zaleski, 1999). The time evolution of the amplitude of the capillary wave for a given numerical box of size 64^2 and for a ratio $h/a_0 = 1.5625$ is shown in fig. 24. The time evolution of the relative error between the computations and the initial-value theory for different grid sizes and for a fixed ratio $h/a_0 = 1.5625$ is shown in fig. 25.

		$1/h$				
		32	64	128	256	512
h/a_0	0.1953125	–	–	–	–	0.0198
	0.39065	–	–	0.0162	0.0145	0.0118
	0.78125	0.0609	0.0062	0.0143	0.0096	0.0064
	1.5625	0.0564	0.0066	0.0127	0.0096	0.0061
	3.125	0.0544	0.0087	0.0145	0.010	0.0063
	6.25	0.0540	0.0101	0.0166	–	–
	12.5	0.0539	–	–	–	–

Table 2: Relative error between the analytical solution and the simulations function of the grid size and of the ratio h/a_0. The density ratio is $\rho_1/\rho_2 = 1$. The error is the r.m.s. of the differences between the numerical and analytical solutions, divided by a_0.

We also performed the same calculations for a different density ratio of $\rho_1/\rho_2 = 10$, for a fixed ratio $h/a_0 = 1.5625$ and different grid sizes. The

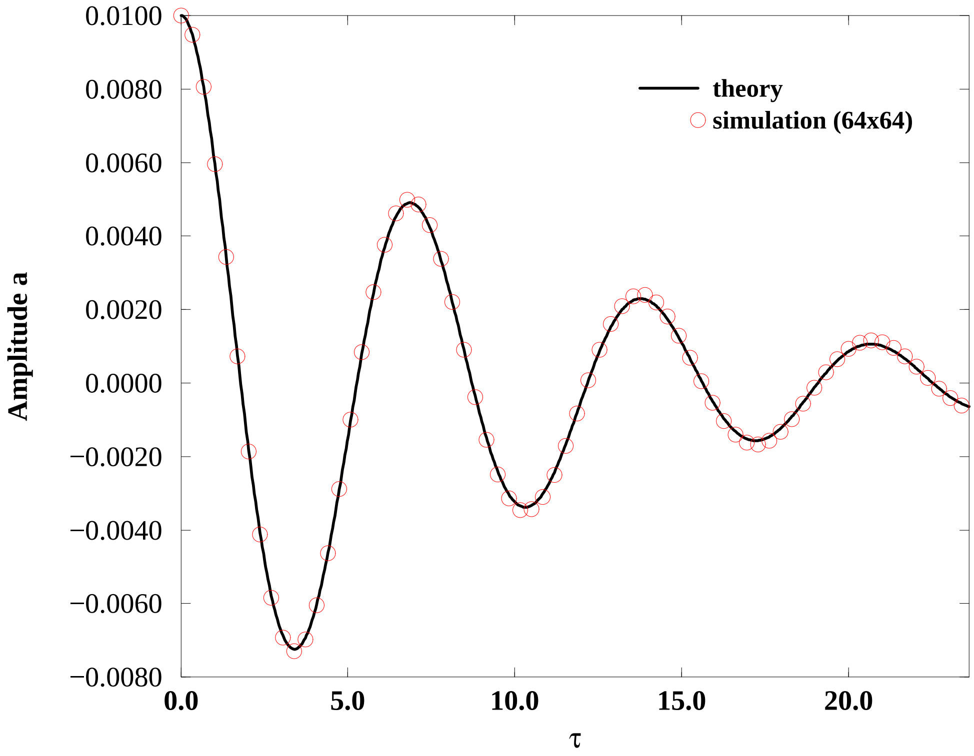

Figure 24: Evolution of the absolute value of the amplitude of the wave versus non-dimensional time $\tau = \omega_0 t$, comparing the analytical solution and the numerical simulation for a box size 64×64. The density ratio is $\rho_1/\rho_2 = 1$.

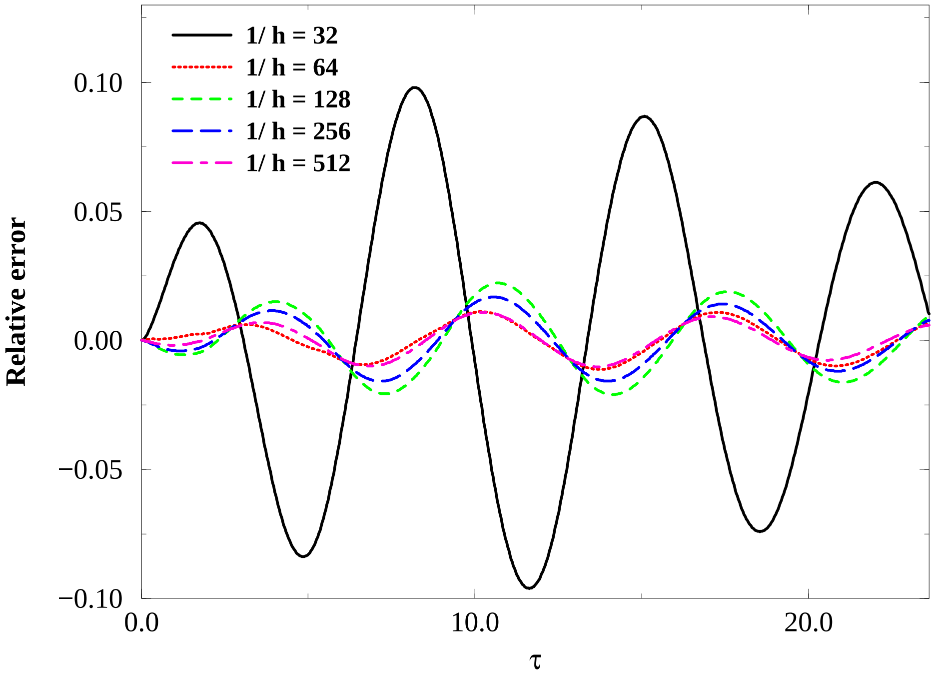

Figure 25: Evolution of the error between the analytical solution and the numerical simulation $a_{theory} - a_{simulation}/a_0$ versus non-dimensional time $\tau = \omega_0 t$ for a fixed ratio $h/a_0 = 1.5625$. Both fluids have the same density $\rho_1 = \rho_2$.

results are summarized in Table 3. For this case, the evolution in time of the relative error for different grid sizes is shown in fig. 26.

$1/h$	Erreur simulation/ théorie
32	0.0735
64	0.0139
128	0.0162
256	0.0129
512	0.0081

Table 3: Relative error between the analytical solution and the simulations for different grid sizes with $\rho_1/\rho_2 = 10$ and $h/a_0 = 1.5625$. The error is the r.m.s. of the differences between the numerical and analytical solutions, divided by a_0.

4.3.5 Spurious currents

A major difficulty with many methods for interface calculations is the existence of the so-called "spurious" or "parasite" currents. These currents are vortices appearing in numerical simulations in the neighborhood of interfaces despite the absence of any external forcing. They are observed with many surface tension simulation methods, including the CSF method, the conservative method of (Lafaurie et al., 1994) or the lattice Boltzmann method (Gunstensen, 1992), in which they were first discovered. They result in a limitation of the range of parameters that may be accessed by the model.

It is difficult to give a systematic expression for the amplitude of spurious currents because they often fluctuate in time, but direct measurements(Lafaurie et al., 1994) yield approximately

$$u_p \simeq 0.01\, \sigma/\mu\,. \tag{82}$$

Taking care to diminish spurious currents (for instance by more accurate estimates of normals or curvatures) yields much smaller values of u_p.

4.3.6 Problems with large surface tension

The simulation methods for flows with interfaces are limited in the range of dimensionless numbers that may be reached. The situation is analogous to that of direct numerical simulations of homogeneous flows, where there is an upper limit for the Reynolds number that grows like a power of the number of grid points.

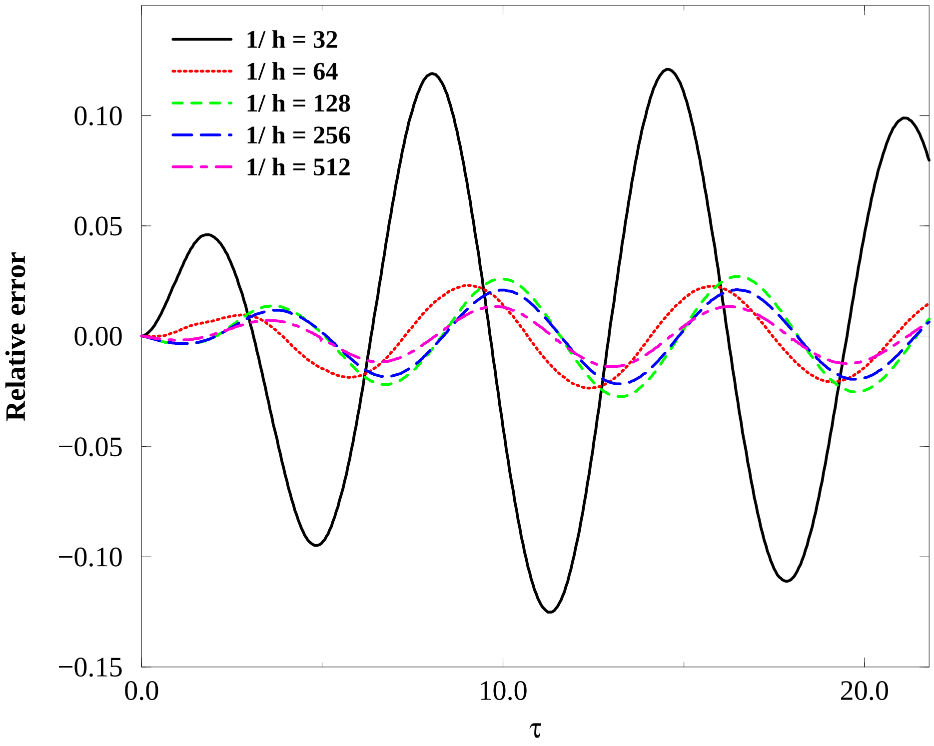

Figure 26: Evolution of the error between the analytical solution and the numerical simulation $a_{theory} - a_{simulation}/a_0$ versus non-dimensional time $\tau = \omega_0 t$ for a fixed ratio $h/a_0 = 1.5625$. The density ratio is $\rho_1/\rho_2 = 10$.

For interface methods, calculations often become difficult when the surface tension becomes large and the density jump is at the same time large. This may happen for bubbles or droplets of small radius R, when surface tension is large compared to viscosity. This means that either the capillary number $\mathrm{Ca} = \mu U/\sigma$ is small or that the *Laplace* number $\mathrm{La} = \sigma\rho R/\mu^2$ is large. Numerical experiments show that at small Ca, but moderate La, no catastrophic instability occurs, and that the only troublesome effects are the spurious currents. On the other hand at large La, parasite currents may grow and become large enough to destroy the interface. This may be easily explained by the connection between La and Reynolds numbers of spurious currents given by eq. (82)

$$\mathrm{La} = 100\mathrm{Re}_p\,, \tag{83}$$

where $\mathrm{Re}_p = u_p R/\nu$. In practice, computations become difficult when $\mathrm{La} \sim 10^6$. This is approximately the value for a 1cm droplet or bubble. Thus this droplet size represents the borderline for present-day simulations.

For larger droplets and Reynolds numbers, one needs to compare surface tension and inertia. At small Weber numbers, $We = U^2\rho R/\sigma$, capillary tension dominates inertial phenomena. Since this happens for smaller R, it may explain why several articles and private communications report difficulties with smaller particles.

4.3.7 Problems with small surface tension

At large Weber numbers, problems also occur because the computed objects (droplets, bubbles, filaments) become very small. In this situations, the breakup phenomenon tends to create smaller structures until the Weber number becomes small enough, at around $We = 10$. If and when these structures reach sizes smaller than the mesh, a loss of accuracy occurs.

First order methods, such as the SOLA-VOF method (Hirt and Nicholls, 1981) are numerically unstable in the absence of surface tension. The interface is progressively destroyed by the generation of floatsam and surface tension is the only way to keep the interface well defined. On the other hand, PLIC methods (Li, 1995) and other more accurate methods such as front tracking avoid this numerical instability. The small structures created at large Weber numbers are often well resolved and have physical meaning.

Moreover, at low Reynolds numbers, small surface tension implies large Ca. This is equally catastrophic, since viscous flow may create cusps in the interface.

5 Tests and applications

5.1 A reconnection test: sessile droplets

Sessile droplets are created by letting the liquid flow very slowly out of a crank. A pendant drop forms, that remains attached to the crank only through a thin liquid bridge, which eventually pinches in several places.

This problem was studied in an inviscid framework by (Schulkes, 1994) and (O guz and Prosperetti, 1993) using a boundary-integral method. Eggers and Dupont (Eggers and Dupont, 1994), obtained an approximation of the full Navier-Stokes equation which is in part a lubrication approximation valid in the limit of slowly-varying thickness $R(z)$. It is a lubrication approximation only in part, because it includes a surface-tension term which is exact, and thus the Eggers-Dupont equation is also valid for static shapes with arbitrary slopes of $R(z)$ such as droplets. With both approaches, (Schulkes, 1994) and (Eggers and Dupont, 1994), it was found a very good agreement with the experiments of Peregrine (Peregrine et al., 1990). More recently, full three-dimensional and two-dimensional axisymmetric viscous simulations have been carried out for this physical situation. The problem is defined by three dimensionless parameters:

- the Bond number $Bo = \rho g r_0^2/\sigma$, where ρ is liquid density, g is gravity, r_0 the radius of the injector;
- the Ohnesorge number Oh based on r_0;
- a Weber number $We = \rho V^2 r_0/\sigma$ based on the velocity V at which the liquid exits the crank.

Details of the calculation are presented in (Gueyffier et al., 1999) and the results show an excellent agreement with the pictures of ref. (Peregrine et al., 1990).

5.2 Sedimentation of droplet arrays in creeping flow

The asymptotical fall velocity of a droplet is given by the classical Hadamard-Rybczynski expression(Batchelor, 1970)

$$\mathbf{U}_{\mathrm{HR}} = \frac{2}{3\mu_{\mathrm{out}}}(\rho_{\mathrm{out}} - \rho_{\mathrm{drop}})a^2 \frac{1+K}{2+3K}\mathbf{g}\,, \tag{84}$$

where μ_{out} and ρ_{out} are the dynamical viscosity and density of the outer fluid and $K = \mu_{\mathrm{out}}/\mu_{\mathrm{drop}}$ is the ratio between the dynamic viscosities of the two

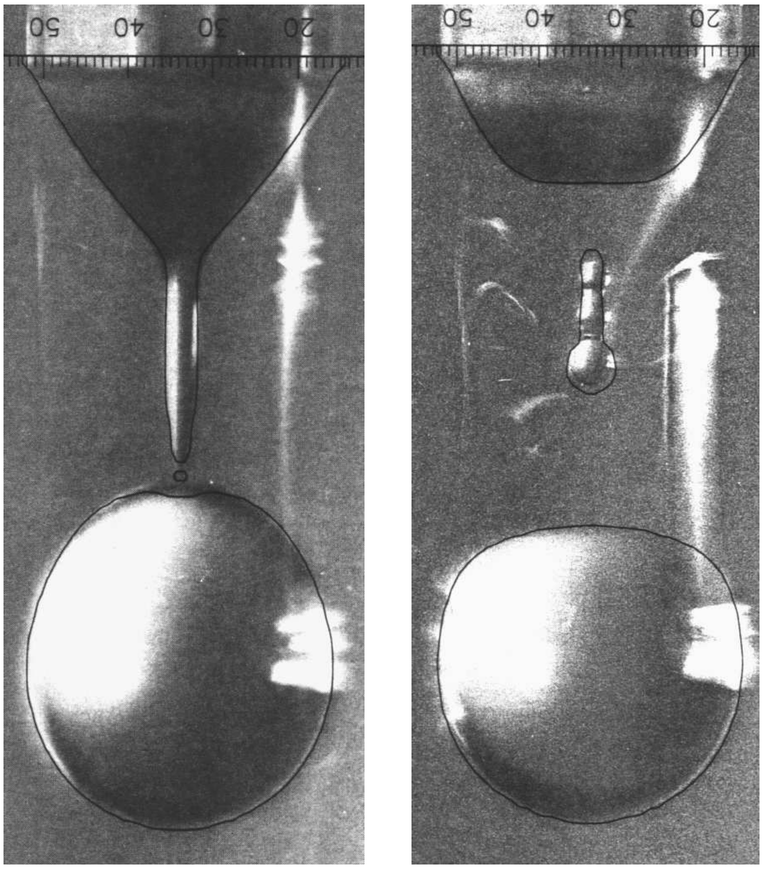

Figure 27: Comparison between an axisymmetric VOF/PLIC calculation and the experiment of (Peregrine et al., 1990).

fluids. Sangani (Sangani, 1987) found solutions of the Stokes equation for *periodic* arrays of droplets. The ratio between the sedimentation velocity of the array of drops U and Hadamard-Rybczynski velocity for a single drop U_{HR} only depends on the viscosity ratio K and on the volume fraction between drops and the outer fluid c.

These theoretical results were compared to three-dimensional calculations with our VOF/PLIC method. The results are shown on Fig. 28. The error increases with K. This is due to the manner in which viscosity is averaged in cut cells. This creates $\mathcal{O}(h)$ errors in the viscous stresses. This problem was addressed in (Coward et al., 1997).

5.3 Kelvin-Helmholtz instability

The phenomenon of droplet peeling on the surface of liquid jets has been abundantly studied (Hoyt and Taylor, 1977; Reitz and Bracco, 1982). These jets are often produced in engine nozzles. The mechanism for the breakup of the jet is quite complex, and difficult to observe because of the very small space and time scales involved. Numerical simulation is therefore well placed to deal with this problem. For fluids of interest in combustion studies (such as the liquid-oxygen/hydrogen or hydrocarbon/air mixtures), the principal difficulties occur from the very large values of the capillary number Ca. This number is about 0.25 in a typical water jet in air at 10m/s water velocity, while it can reach the value 10 in hydrocarbons or cryogenic fluids. Figure 29 shows an example of such a peeling obtained for Ca $= 0.02$, while figure 30 shows an example for Ca $= 1$. The simulations give very different results. In the second case structures of very small size are formed because of the systematic stretching of a thin filament of liquid. The precision of the calculation is limited by the formation of these very small structures. Our three-dimensional simulations analyze the response to spanwise perturbations of the above two-dimensional base-flow (Zaleski et al., 1996). The pinching mechanism by which liquid droplets detach from the edges of sheets in two-dimensional flow is not necessarily the realistic three-dimensional regime. We have been able so far to distinguish two scenarios by which three-dimensional flow sets in. For small three-dimensional perturbations, the simulation remains two-dimensional until the sheet breaks and a cylinder pinches off. Subsequently, the capillary instability of jets gives three-dimensional structure to the flow. In this case, the two dimensional simulations are very useful to predict the evolution of the flow and the droplet size. In contrast, for higher three-dimensional perturbations, a different scenario is observed, as shown on Figure 31 (This simulation took about 48 hours to complete on an IBM RS6000/370). The rim-like edge concentrates in a protruding finger that

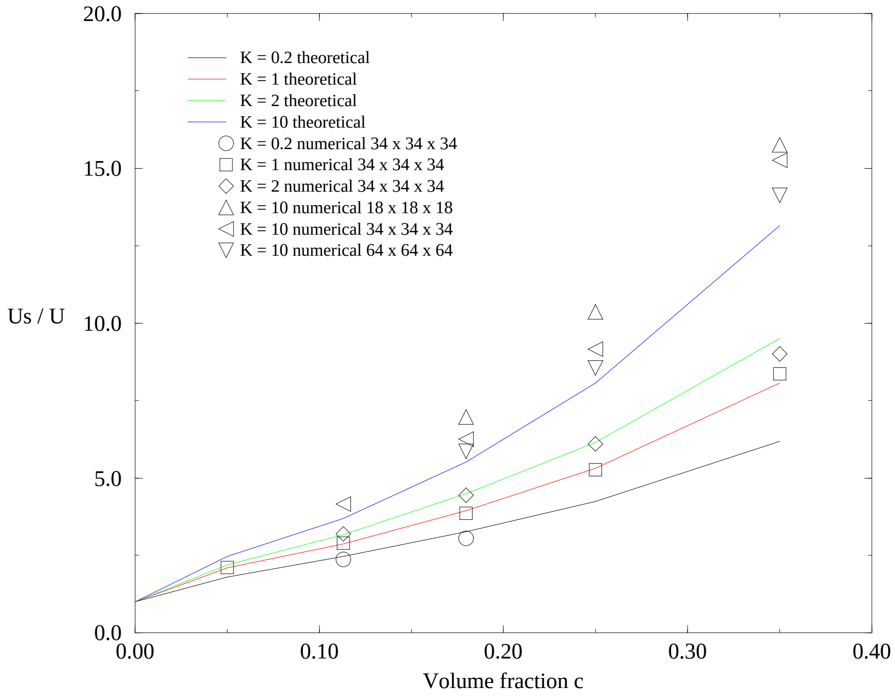

Figure 28: Ratio between sedimentation velocity of an infinite array of drops and Stokes velocity for a single drop.

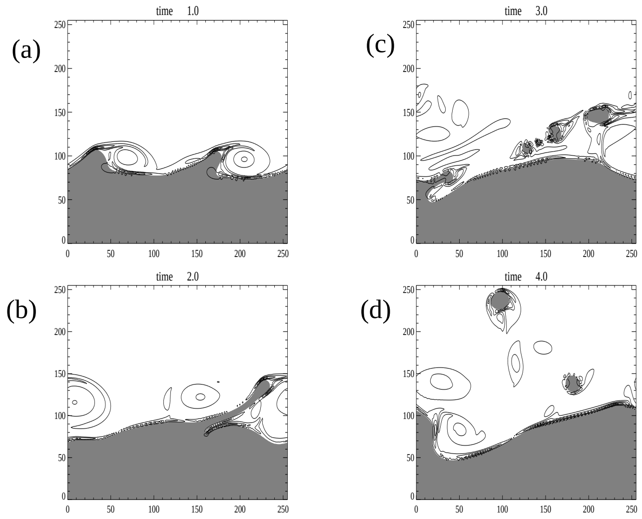

Figure 29: Droplet formation in a 2D sheared layer. The parameters are $\rho_L/\rho_G = 10$, $Re_G = 7500$ and $We_G = 150$. The liquid phase is the grey area. The lines are iso-vorticity levels.

will be subject to the capillary instability. However, the unstable cylinder is now streamwise. The formation of streamwise filaments or fingers is observed in real experiments on shear layers (Raynal et al., 1995) and it is also reminiscent of the the crown formation in droplet impact experiments (Yarin and Weiss, 1995).

6 Conclusion

In the author's opinion, the main progress witnessed over the past ten years is the advent of many three-dimensional calculations. Two-dimensional calculations have also matured, producing either highly accurate results or calculations over impressively large grids.

The one new method that appeared is level sets. It is seducing by its simplicity, but has not yet produced the wide range of results, especially in three-dimensions, achieved by older methods. The Volume of Fluid method has been considerably improved by the systematic use in the scientific literature of the higher order piecewise linear interface calculation method.

There are still important calculations that have not yet been done. For instance, there is no three dimensional calculation of a falling drop or rising bubble in the difficult air/water conditions and in the non-trivial regimes where axial symmetry does not hold. Many complex flows, such as atomiz-

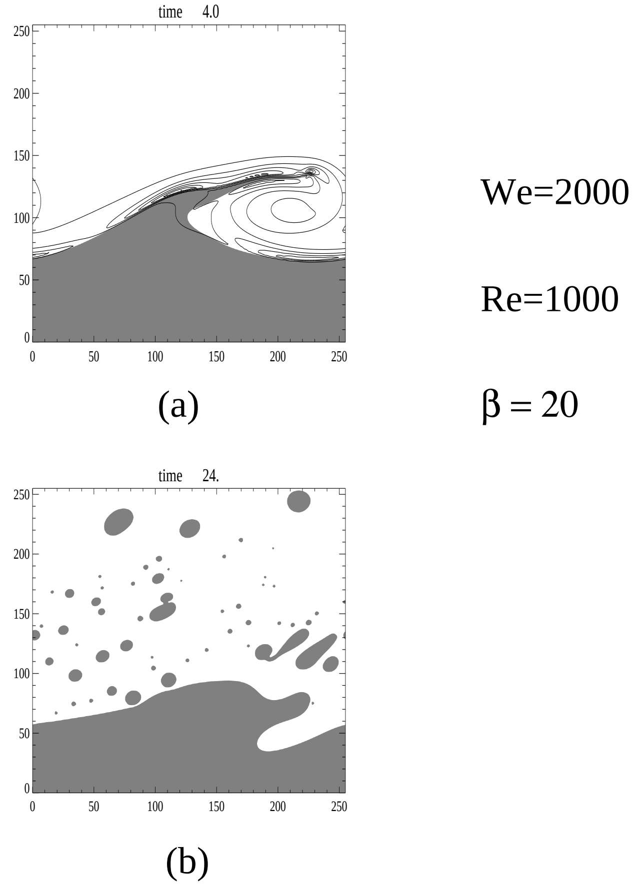

Figure 30: Droplet formation at higher capillary and Weber numbers. The intermediate steps are not shown. The level lines of the vortices are also omitted on figure (b) to avoid overcrowding the plot.

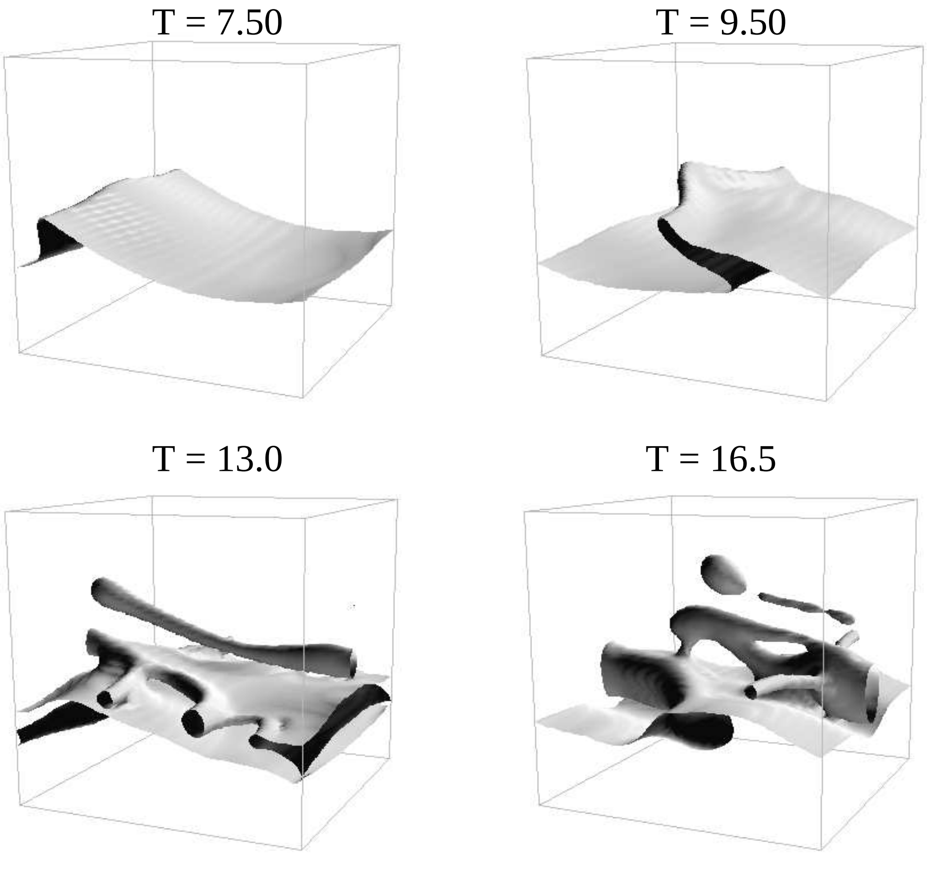

Figure 31: Breakup of the interface through a secondary instability of the sheet. $\rho_L/\rho_G = 10$, $Re = 1000$ and $We = 300$.

ing jets, splashing droplets or breaking waves, have been studied only in a preliminary way. Finally, for some flows quantitative results are difficult to get, in particular, agreement between simulations and linear theory for shear flow instabilities.

For engineering applications, new methods need to be developed that could adapt to complex geometries, such as combustors and nozzles to cite just two of a whole world of examples.

It is the author's opinion that these difficulties should soon be resolved. This would allow these methods to connect directly with scientific problems and engineering applications in multiphase flow. From there the simulation of interfaces could move on to incorporate more complex physics, such as models of intermolecular forces, complex surface rheology, and the transport and effects of tensio-active molecules.

References

Aleinov, I. and Puckett, E. G. (1995). Computing surface tension with high-order kernels. In Oshima, K., editor, *Proceedings of the 6th International Symposium on Computational Fluid Dynamics*, pages 6–13, Lake Tahoe, CA. May be obtained from the author's web page at http://math.math.ucdavis.edu/ egp/.

Aris, R. (1962). *Vectors, tensors and the basic equations of fluid mechanics.* Prentice-Hall,INC.

Ashgriz, N. and Poo, J. Y. (1991). FLAIR: Flux line-segment model for advection and interface reconstruction. *J. Comput. Phys.*, 93:449–468.

Batchelor, G. K. (1970). *An introduction to fluid dynamics.* Cambridge Univ. Press.

Bell, J., Dawson, C., and Shubin, G. (1990). An unsplit, higher order godunov method for scalar conservation laws in multiple dimensions. *J. Comput.Phys.*, 74:171–200.

Benzi, R., Succi, S., and Vergassola, M. (1992). The lattice Boltzmann equation: Theory and applications. *Phys. Rep.*, 222:145–197.

Brackbill, J., Kothe, D. B., and Zemach, C. (1992). A continuum method for modeling surface tension. *J. Comput. Phys.*, 100:335–354.

Chorin, A. J. (1980). Flame advection and propagation algorithms. *J. Comput. Phys.*, 35:1–11.

Collela, P. (1990). Multidimensional upwind methods for hyperbolic conservation laws. *J. Comput. Phys.*, 87:171–200.

Cortelezzi, L. and Prosperetti, A. (1981). Small amplitude waves on the surface of a layer of a viscous liquid. *Quaterly Appl. Math.*, 38:375–388.

Coward, A. V., Renardy, Y. Y., Renardy, M., and Richards, J. R. (1997). Temporal evolution of periodic disturbances in two-layer couette flow. *J. Comput. Phys.*, 132:346–361.

de Gennes, P. G. (1985). Wetting: statics and dynamics. *Rev. Mod. Phys*, 57:827–863.

DeBar, R. (1974). Fundamentals of the KRAKEN code. Technical report.

Eggers, J. (1993). Universal pinching of 3D axisymmetric free-surface flow. *Phys. Rev. Lett.*, 71:3458–3461.

Eggers, J. (1997). Nonlinear dynamics and breakup of free-surface flows. *Rev. Mod. Phys.*, 69:865–929.

Eggers, J. and Dupont, T. D. (1994). Drop formation in a one-dimensional approximation of the Navier-Stokes equation. *J. Fluid Mech.*, 262:205–221.

Floryan, J. M. and Rasmussen, H. (1989). Numerical methods for viscous flow with moving boundaries. *Appl. Mech. Rev.*, 42:323–340.

Glimm, J., Bryan, O. M., Menikoff, R., and Sharp, D. (1986). Front tracking applied to Rayleigh–Taylor instability. *SIAM J. Sci. Stat. Comput.*, 7:230–251.

Glimm, J., McBryan, O., Menikoff, R., and Sharp, D. H. (1987). Front tracking applied to rayleigh-taylor instability. *SIAM J. Sci. Stat. Comput.*, 7:230–251.

Gueyffier, D., Nadim, A., Li, J., Scardovelli, R., and Zaleski, S. (1999). Volume of fluid interface tracking with smoothed surface stress methods for three-dimensional flows. *J. Comput. Phys.*, 152:423–456.

Gunstensen, A. K. (1992). *Lattice-Boltmann Studies of Multiphase Flow Through Porous Media.* PhD thesis, Massachusetts Institute of Technology.

Hirt, C. W. and Nicholls, B. D. (1981). Volume of fluid (VOF) method for the dynamics of free boundaries. *J. Comput. Phys.*, 39:201–225.

Hoyt, J. W. and Taylor, J. (1977). Waves on water jets. *J. Fluid Mech.*, 83:119–127.

Kothe, D. B. and Mjolsness, R. C. (November 1992). RIPPLE: A new model for incompressible flows with free surfaces. *AIAA journal*, 30:2694–2700.

Lafaurie, B., Nardone, C., Scardovelli, R., Zaleski, S., and Zanetti, G. (1994). Modelling merging and fragmentation in multiphase flows with SURFER. *J. Comput. Phys.*, 113:134–147.

LeVeque, R. (1996). An unsplit, higher order godunov method for scalar conservation laws in multiple dimensions. *SIAM J. Numer. Anal.*, 33:627–665.

Li, J. (1995). Calcul d'interface affine par morceaux (piecewise linear interface calculation). *C. R. Acad. Sci. Paris, série IIb, (Paris)*, 320:391–396.

Longuet-Higgins, M. S. (1998). Vorticity and curvature at a free surface. *J. Fluid Mech.*, 356:149–153.

Mc Hyman, J. (1984). Numerical methods for tracking interfaces. *Physica D*, 12:396–407.

Miller, G. H. and Puckett, E. G. (1996). A high-order godunov method for multiple condensed pahses. *J. Comput. Phys.*, 128:134–164.

Nichols, B. D., Hirt, C. W., and Hotchkiss, R. S. (August 1980). SOLA-VOF: A solution algorithm for transient fluid flow with multiple free boundaries. *Technical Report LA-8355, Los Alamos National Laboratory.*

Noh, W. and Woodward, P. (1976). SLIC (simple line interface calculation). In van de Vooren, A. and Zandbergen, P., editors, *Proceedings, Fifth International Conference on Fluid Dynamics*, volume 59 of *Lecture Notes in Physics*, pages 330–340, Berlin. Springer.

O guz, H. N. and Prosperetti, A. (1993). Dynamics of bubble growth and detatchment from a needle. *J. Fluid Mech.*, 257:111–145.

Parker, B. J. and Youngs, D. L. (February 1992). Two and three dimensional eulerian simulation of fluid flow with material interfaces. Technical report.

Peregrine, D. H., Shoker, G., and Simon, A. (1990). The bifurcation of liquid bridges. *J. Fluid. Mech.*, 212:25–39.

Peyret, R. and Taylor, T. D. (1983). *Computational Methods for Fluid Flow*. Springer Verlag, New York/Berlin.

Pilliod Jr, J. E. and Puckett, E. G. (1997). Second-order accurate volume-of-fluid algorithms for tracking material interfaces. Technical report, Lawrence Berkeley National Laboratory. No. LBNL-40744, also submitted to J. Comput. Phys.

Popinet, S., Scardovelli, R., and Zaleski, S. (1997). Code de suivi de volume ciam en maillage irregulier. Internal lmm report, Laboratoire de Modélisation en Mécanique, UMR CNRS 7607, Université Pierre et Marie Curie.

Popinet, S. and Zaleski, S. (1998). Simulation of axisymmetric free-surface viscous flow around a non-spherical bubble in the sonoluminescence regime. In *Proceedings of ICMF98*.

Popinet, S. and Zaleski, S. (1999). A front tracking algorithm for the accurate representation of surface tension. *Int. J. Numer. Meth. Fluids*, 30:775–793.

Prosperetti, A. (1981). Motion of two superposed viscous fluids. *Phys. Fluids*, 24:1217–1223.

Puckett, E. G. (1991). A volume-of-fluid interface tracking algorithm with applications to computing shock wave refraction. In Dwyer, H., editor, *Proceedings of the 4th International Symposium on Computational Fluid Dynamics,Davis, CA, 1991*, pages 933–938.

Puckett, E. G., Almgren, A. S., Bell, J. B., Marcus, D. L., and Rider, W. J. (1997). A high-order projection method for tracking fluid interfaces in variable density incompressible flows. *J. Comp. Phys.*, 130:269–282.

Puckett, E. G. and Saltzman, J. S. (1992). A 3D adaptive mesh refinement algorithm for interfacial gas dynamics. *Physica D*, 60:84–93.

Raynal, L., Villermaux, E., and Hopfinger, E. J. (1995). Couche de mélange eau/air à grands rapports de quantité de mouvement. *Rapport Final, Contrat SEP* n° *910023*.

Reitz, D. and Bracco, F. (1982). Mechanism of atomisation of a liquid jet. *Physics of Fluids*, 25:1730–1742.

Rider, W. J. and Kothe, D. B. (1995). Stretching and tearing interface tracking methods. AIAA paper 95-1717.

Rider, W. J. and Kothe, D. B. (1998). Reconstructing volume tracking. *J. Comput. Phys.*, 141:112–152. Euler split and unsplit, alternating implicit/explicit volume expansion factor.

Rothman, D. H. and Zaleski, S. (1994). Lattice-gas models of phase separation: interfaces, phase transitions, and multiphase flow. *Rev. Mod. Phys.*, 66:1417–1479.

Rothman, D. H. and Zaleski, S. (1997). *Lattice-gas cellular automata*. Cambridge University Press, Cambridge, UK.

Sangani, A. S. (July 1987). Sedimentation in ordered emulsions of drops at low Reynolds numbers. *J. of Appl. Math. and Physics (ZAMP)*, 38:542–556.

Schulkes, R. M. S. (1994). The evolution and bifurcation of a pendant drop. *J. Fluid Mech.*, 278:83–100.

Sethian, J. A. (1996). *Level Set Methods*. Cambridge University Press.

Shyy, W., Udaykumar, H., Rao, M. M., and Smith, R. W. (1996). *Computational fluid dynamics with moving boundaries*. Taylor and Francis, London.

Stone, H. A. (1994). Dynamics of drop deformation and breakup in viscous fluids. *Annual Reviews of Fluid Mechanics*, 26:65–102.

Sussman, M. and Smereka, P. (1997). Axisymmetric free boundary problems. *J. Fluid Mech.*, 341:269–294.

Sussman, M., Smereka, P., and Osher, S. (1994). A level set approach for computing solutions to incompressible two-phase flow. *J. Comput. Phys.*, 114:146–159.

Torrey, M. D., Cloutman, L. D., Mjolsness, R. C., and Hirt, C. W. (December 1985). NASA-VOF2D: A computer program for incompressible with free surfaces. *Technical Report LA-101612-MS, Los Alamos National Laboratory*.

Torrey, M. D., Mjolsness, R. C., and Stein, L. R. (July 1987). NASA-VOF3D: A three-dimensional computer program for incompressible with free surfaces. *Technical Report LA-11009-MS, Los Alamos National Laboratory*.

Tryggvason, G. and Unverdi, S. O. (1990). Computations of three-dimensional Rayleigh-Taylor instability. *Phys. Fluids*, 2:656–659.

Unverdi, S. O. and Tryggvason, G. (1992a). Computation of multifluid flow. *Physica D*, 60:70–83.

Unverdi, S. O. and Tryggvason, G. (1992b). A front-tracking method for viscous, incompressible, multi-fluid flows. *J. Comput. Phys.*, 100:25–37.

Yarin, A. L. and Weiss, D. A. (1995). Impact of drops on solid surfaces : self-similar capillary waves, and splashing as a new type of kinematic discontinuity. *J. Fluid Mech.*, 283:141–173.

Zaleski, S., Li, J., Scardovelli, R., and Zanetti, G. (1996). Direct simulation of multiphase flows with density variations. In *colloque IUTAM "Variable Density Low Speed Turbulent Flows"*. Kluwer.